Master Thesis

Czech
Technical
University
in Prague

F3

Faculty of Electrical Engineering
Department of Radio Engineering

Fundamental Bounds on Magnetic Levitation and Magnetic Confinement

Jakub Liška

Supervisor: Lukáš Jelínek
Supervisor–specialist: Konstantin R. Simovski, Miloslav Čapek
Field of study: Open Electronic Systems
Subfield: RF and DSP Engineering
May 2021

Acknowledgements

I would like to thank Lukáš Jelínek for an excellent management of this thesis, perfect cooperation, kindliness, and provided expertise. Thanks goes also to Konstantin Simovski, co-supervisor at Aalto University. Chiefly, I would like to thank all members of the Antenna Toolbox for MATLAB (AToM) development team and members of the Computational Electromagnetism group at the Department of Electromagnetic Field for the developed computational tools, namely, Miloslav Čapek, also for helpful remarks during thesis elaboration. Furthermore, thanks go to my family and friends for expressing their support and creating a nice environment not only during the process of writing, but also during the whole period of my studies.

Declaration

I declare that I completed the presented thesis independently and that all used sources are quoted in accordance with the Methodological instructions that cover the ethical principles for writing an academic thesis.

In Prague, 21st May 2021

„Prohlašuji, že jsem předloženou práci vypracoval samostatně, a že jsem uvedl veškeré použité informační zdroje v souladu s Metodickým pokynem o dodržování etických principů při přípravě vysokoškolských závěrečných prací.“

V Praze, 21. květen 2021

Abstract

The thesis deals with the problem of magnetic levitation and magnetic confinement, mainly with the development of fundamental bounds on these phenomena and their comparison with the performance of commonly used levitation and confinement devices. Local approximations are introduced, which allows the proposal of scalar metrics judging the performance. Optimization problems for the fundamental bounds are established in this formalism. Computational tools are introduced and implemented to evaluate performance metrics and determine fundamental bounds for arbitrary current supporting regions. The optimization algorithms are also introduced and implemented. The aforementioned tools are applied to find the fundamental bound on magnetic levitation for a circular plate, which is then compared to the performance of the two selected realizations. Fundamental bounds on magnetic confinement are evaluated for current support in the form of a sphere, cylinder, and cube. Performance of magnetic traps: baseball, Ioffe-Pritchard, hexapole, and quadrupole are compared with the fundamental bound.

Keywords: magnetic levitation, magnetic containment, magnetic traps, fundamental bounds

Supervisor: Lukáš Jelínek
Faculty of Electrical Engineering,
Czech Technical University in Prague,
Technická 1902/2,
Praha 6

Abstrakt

Práce se zabývá problematikou magnetické levitace a magnetického zadržení, především principiálními limity těchto jevů a jejich porovnáním s výkonem běžně používaných levitačních a zadržovacích zařízení. Jsou zavedeny lokální aproximace, které umožňují navrhnout skalární metriky posuzující jejich výkon. V navrženém formalismu jsou stanoveny optimalizační problémy pro principiální omezení. Jsou zavedeny a implementovány výpočetní nástroje pro vyhodnocení metrik výkonnosti a určení principiálních limitů pro libovolné proudové nosné oblasti. Jsou rovněž zavedeny a implementovány optimalizační algoritmy. Výše uvedené nástroje jsou použity k nalezení principiálních omezení magnetické levitace pro kruhovou desku, která je následně porovnána s výkonností dvou vybraných realizací. Principiální omezení magnetického zadržování jsou vyhodnoceny pro proudovou oblast ve tvaru koule, válce a krychle. Výkonnost magnetických pastí: baseballové, Ioffeovy-Pritchardovy, hexapólové a kvadrupólové je porovnána s principiální mezí.

Klíčová slova: magnetická levitace, magnetické zadržování, magnetické pasti, principiální limity

Překlad názvu: Principiální omezení magnetické levitace a magnetického zadržování

Contents

Figures

Tables

Chapter 1

Introduction

The phenomenon of levitation is a gravity compensation problem, which has always attracted attention: illusionists let objects float freely in mid-air by "supernatural forces", while applied physics successfully attempt to levitate maglev trains which are then capable of moving at speeds as high as 500 km/h [1–4]. Levitation can be achieved in different ways: a jet of gas (aerodynamic levitation of laser-heated solids [5], indoor skydiving [6]), intense sound waves (structure measurements on low-temperature liquid droplets [7]) or laser beams (observation of light scattering from non-spherical particles [8]) and notably for this thesis, conductors can levitate in strong time-varying magnetic fields, charged particles in quasi-static electric fields, diamagnets and neutral atoms in a quasi-static magnetic field, magnets above superconductors or vice versa [1,3]. This thesis focuses on levitation induced by a quasistatic magnetic field formed by a properly shaped surface current density.

The first goal of this thesis is to study physical bounds on magnetic levitation within the view of classical electrodynamics. Magnetic levitation is achieved by the spatial distribution of magnetic field magnitude, which can exhibit a local minimum in a source-free region [1,3,9–11], [12, section 10.1.4] in which objects made of material with negative magnetic susceptibility, or objects with negative magnetic polarisability can levitate [2,3,12–14], see the detailed analysis in chapter 2. This is the case of diamagnets such as water and living matter, with the widely known example of a levitating frog shown in figure 1.1, or superconductors [1,10,13,14].

The second goal of this thesis is a study of physical bounds to magnetic confinement, which results from similar conditions as magnetic levitation. The fundamental difference is that the magnetic field is used to spatially localize microscopic particles and does not fight against gravity but against thermal excitation. The particles at room temperature move at speeds of the

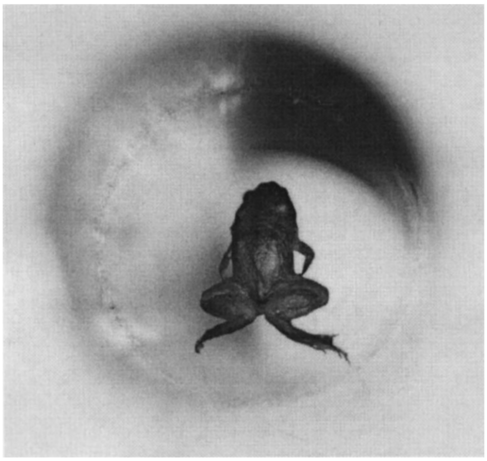

Figure 1.1: Frog levitated in stable zone of a 16 T magnet [10, 14].

order 300 m/s, the speed of sound, thermal velocity is decreased by cooling. The deceleration of atoms is done by a laser beam before trapping them by magnetic field [11]. The phenomenon of magnetic confinement (localization in a potential well) establishes the basis for modern ultracold physics and its applications, quantum information processing, quantum metrology, quantum objects, quantum optics, gravimetry, or high-resolution spectroscopy [9, 15]. Apart from applications, magnetic confinement indicates many similarities with magnetic levitation, mainly that the confining potential is attributed to the minimum of magnetic field magnitude, where the particles are trapped [1, 3, 9–11], [12, section 10.1.4].

Chapter 2

Assumptions & Restrictions

This chapter introduces the requirements, assumptions, and restrictions on the description of magnetic levitation and confinement that are used throughout this thesis. Apart from physical requirements like low field seekers and magnetic precession, assumptions for local approximations leading to the application of second-order Taylor polynomial to the potential energy are established.

Since this thesis is solely focused on magnetic levitation and confinement in quasistatic settings, only the vacuum surrounding is considered with ε_0 denoting permittivity of vacuum and μ_0 denoting the permeability of vacuum.

An essential assumption used in the thesis is that the objects attracted, repelled by the magnetic field are much smaller than the important space changes of the magnetic field. This allows to use a local approximation of the magnetic potential energy [12, section 12.4.2]

$$\phi = -\gamma \boldsymbol{m} \cdot \boldsymbol{B}, \tag{2.1}$$

where γ is a positive scaling constant, $\boldsymbol{m}$ is a magnetic dipole moment of the trapped or levitating particle and $\boldsymbol{B}$ is magnetic field without the presence of the particle. This local description also allows to expand potential energy ϕ into second-order Taylor polynomial [16, section 4.3], [17, section 8.7] as

$$\phi(\boldsymbol{\rho}) \approx \phi(\boldsymbol{r}_0) + \boldsymbol{g}^{\mathrm{T}} \boldsymbol{\rho} + \frac{1}{2} \boldsymbol{\rho}^{\mathrm{T}} \mathbf{H} \boldsymbol{\rho}, \quad \boldsymbol{\rho} = \boldsymbol{r} - \boldsymbol{r}_0 \tag{2.2}$$

where $\boldsymbol{g}$ denotes gradient of potential energy at point $\boldsymbol{r}_0$,

$$g_i = \left. \frac{\partial \phi}{\partial i} \right|_{\boldsymbol{r}=\boldsymbol{r}_0}, \tag{2.3}$$

and $\mathbf{H}$ is Hessian matrix evaluated at the same point, the elements of which read

$$H_{ij} = \left. \frac{\partial^2 \phi}{\partial j \partial i} \right|_{\boldsymbol{r}=\boldsymbol{r}_0}, \tag{2.4}$$

with ∂i and ∂j denoting derivatives with respect to Cartesian coordinates, i.e. $i, j \in \{x, y, z\}$. Hessian matrix is symmetric thanks to the interchangeability of derivatives. The quadratic approximation (2.2) is used to quantify the properties of the magnetic potential wells.

The aforementioned local description is adequate for microscopic objects (the most important case of magnetic confinement) or mesoscopic objects. Macroscopic objects of general shape and size cannot be described in this way. The description of the action of the magnetic force on an extended body will demand to precisely evaluate the current densities flowing in it, back-reaction of the body, the full Lorentz's force, and, importantly, also nontrivial kinematics. This will immensely complicate the mathematical description. For this reason, this thesis will solely focus on problems where local approximation is sufficient and the main goal of this thesis is to provide a basic appraisal of magnetic levitation and confinement in which the approximation is convenient.

Within the local approximation (2.1), this thesis assumes two types of dipole moments: induced and permanent. The induced dipole is assumed in the form [12, section 13.6]

$$\boldsymbol{m} = \alpha \boldsymbol{B} \tag{2.5}$$

with isotropic polarisability α to avoid the need to study the spatial orientation of the levitating body. The potential energy (2.1) in this case reads

$$\phi = -\frac{\alpha}{2} |\boldsymbol{B}|^2, \tag{2.6}$$

with scaling constant $\gamma = -1/2$. Since the magnitude of the magnetic field can only exhibit local minimum [1,3,9–11], [12, section 10.1.4], the phenomena of magnetic levitation and confinement demand negative magnetic polarizability $\alpha < 0$, i.e., diamagnetic objects, in which the induced current densities arrange themselves to create magnetic field opposing the excitation. The superconducting body is a particular case of a diamagnet [12, section 13.6.6] as is a highly conducting body exposed to an alternating magnetic field.

A permanent magnetic dipole is a vector of constant magnitude m, which can, however, precess around the direction of the magnetic field at an angle and at angular velocity ω_{p} determined by the field magnitude [12, section 12.4.5]. Here we adopt the adiabatic approximation [18] in which the precessing dipole only experiences a slowly rotating magnetic field around its local main direction. Macroscopic permanent magnetic dipoles always arrange themselves in parallel with external magnetic field and can not thus be levitated or trapped by magnetic field [12, application 12.2]. Since there is very little interest to levitate microscopic particles, throughout this thesis, it is therefore assumed that permanent magnetic dipoles are only to be confined.

Neutral atoms prepared in specific (low field seeking) Zeeman sub-levels [9, 19], provide a permanent magnetic dipole antiparallel to the magnetic field main direction. Such neutral atoms can therefore be trapped in the magnetic field which is used in preparing them for Bose-Einstein condensation [9,19], [12, application 12.2].

When a precessing microscopic magnetic dipole is placed in a magnetic field, the time-averaged magnetic moment reads [18]

$$\boldsymbol{m} = -m\frac{\boldsymbol{B}}{|\boldsymbol{B}|}, \tag{2.7}$$

its direction is antiparallel to magnetic field and $m = |\boldsymbol{m}|$ is the moment magnitude. The magnetic potential energy is given by (2.1) with scaling $\gamma = 1$ and reads

$$\phi = m|\boldsymbol{B}|, \tag{2.8}$$

which is also called adiabatic approximation to magnetic potential energy [18]. This approximation is justified when vibrational frequency ω_v of the dipole is small compared to ω_p which is the case in most practical scenarios [9, 18, 19]. The condition for vibrational and precession frequencies implies the necessity of enough strong magnetic field at the position of levitation or trapping. This is nevertheless desired property, as zero-field at the point of trapping increases the probability of non-adiabatic transitions leading to an escape of the particles via spin-flip Majorana transition [9, 19].

Chapter 3

Problem Analysis

This chapter provides a detailed analysis of magnetic levitation and confinement using the squared magnitude of the magnetic field, which is then used to write the magnetic potential energy (2.1) as second-order Taylor polynomial (2.2). This treatment serves to unify the description of induced (2.6) and permanent (2.8) magnetic dipole. The chapter also contains an introduction to the fundamental bounds of magnetic levitation and confinement.

Regardless of the nature of the dipole, the force it feels in an external magnetic field reads element-wise [12, section 12.4.1]

$$F_i = \boldsymbol{m} \cdot \frac{\partial \boldsymbol{B}}{\partial i} \tag{3.1}$$

which also corresponds to the minus gradient of potential energy ϕ [20, section 2.6] for both models introduced in chapter 2. The linear term in Taylor expansion (2.2) is therefore related to force. The quadratic term in (2.2) is defined via the Hessian matrix (2.4), which reads element-wise

$$H_{ij} = -\frac{\partial F_i}{\partial j} = -\boldsymbol{m} \cdot \frac{\partial^2 \boldsymbol{B}}{\partial j \partial i} - \frac{\partial \boldsymbol{m}}{\partial j} \cdot \frac{\partial \boldsymbol{B}}{\partial i}. \tag{3.2}$$

While the role of force (3.1) in the analysis is clear, the Hessian matrix deserves an explanation. The properties of the Hessian matrix are entirely determined by its eigenpairs coming from eigenvalue problem

$$\mathbf{H} \boldsymbol{q}_i = \lambda_i \boldsymbol{q}_i, \quad i \in \{1, 2, 3\}, \tag{3.3}$$

where λ_i is an eigenvalue and $\boldsymbol{q}_i$ is an associated eigenvector. "Second derivative test" says that, if there is zero force at a given point and the Hessian matrix is positive definite, the potential function has local minimum at that point [16, section 4.3], [17, section 11.7]. Definiteness of a matrix is given by its eigenvalues: all of them are positive for positive definite matrix, none of them are negative for positive semi-definite and analogously for negative semi-definite and negative definite matrices [21, section 7.2]. Furthermore, the Hessian matrix eigenvalues determine the force derivatives (potential curvature) along the eigenvectors.

In order to simplify the analysis and to unify the cases of polarizable and permanent dipoles, it is advantageous to introduce auxiliary quantities defined as follows[1]. The squared magnitude of the magnetic field is denoted as

$$\Phi = B^2 = \boldsymbol{B} \cdot \boldsymbol{B}, \tag{3.4}$$

its gradient is denoted $\boldsymbol{\Gamma}$, the components of which read

$$\Gamma_i = \left(\frac{\partial \boldsymbol{B}}{\partial i} \cdot \boldsymbol{B} + \boldsymbol{B} \cdot \frac{\partial \boldsymbol{B}}{\partial i} \right), \tag{3.5}$$

and the Hessian matrix of the function Φ is denoted as $\boldsymbol{\Xi}$ with elements

$$\Xi_{ij} = \left(\frac{\partial^2 \boldsymbol{B}}{\partial j \partial i} \cdot \boldsymbol{B} + \boldsymbol{B} \cdot \frac{\partial^2 \boldsymbol{B}}{\partial j \partial i} + \frac{\partial \boldsymbol{B}}{\partial i} \cdot \frac{\partial \boldsymbol{B}}{\partial j} + \frac{\partial \boldsymbol{B}}{\partial j} \cdot \frac{\partial \boldsymbol{B}}{\partial i} \right). \tag{3.6}$$

The arbitrariness of $\boldsymbol{\Gamma}$ and $\boldsymbol{\Xi}$ is further restricted by the properties of the magnetic field in source free region,

$$\nabla \cdot \boldsymbol{B} = 0, \tag{3.7}$$

$$\nabla \times \boldsymbol{B} = 0, \tag{3.8}$$

$$\Delta \boldsymbol{B} = 0, \tag{3.9}$$

or element-wise

$$\sum_i \frac{\partial B_i}{\partial i} = 0, \tag{3.10}$$

$$\frac{\partial B_i}{\partial j} - \frac{\partial B_j}{\partial i} = 0, \tag{3.11}$$

$$\sum_i \frac{\partial^2 B_i}{\partial i^2} = 0. \tag{3.12}$$

If the magnetic field is used as an optimization variable, these last relations have to be considered as constraints. In this thesis, however, the magnetic field is generated by the current density, which is the degree of freedom in optimization, so equations (3.7)–(3.9) are automatically satisfied through the use of an appropriate Green's function (Biot-Sawart's law), shown later in section 4.1.

Using (3.4)–(3.6), the description of the magnetic field interaction with induced and permanent dipole models from chapter 2 can be written as:

---

[1] All expressions are written in symmetric form suitable for subsequent optimization process.

- induced magnetic dipole:

$$\phi = -\frac{\alpha}{2}\Phi, \tag{3.13}$$

$$F_i = \frac{\alpha}{2}\Gamma_i, \tag{3.14}$$

$$H_{ij} = -\frac{\alpha}{2}\Xi_{ij}, \tag{3.15}$$

- permanent magnetic dipole:

$$\phi = \mu\sqrt{\Phi}, \tag{3.16}$$

$$F_i = -\frac{\mu^2}{2\phi}\Gamma_i, \tag{3.17}$$

$$H_{ij} = \frac{\mu^2}{2\phi}\Xi_{ij} - \frac{1}{\phi}F_iF_j. \tag{3.18}$$

Knowledge of these quantities allows the analysis of levitation and confinement provided in the following sections.

3.1 Levitation

The phenomenon of levitation is a fight against gravity by other forces. Suppose gravity antiparallel to z-axis. Then the total potential energy perceived by the magnetic dipole reads

$$\phi_{\mathrm{T}} = \phi + mgz + \phi_0, \tag{3.19}$$

where m is the mass of the dipole, g is the gravitational acceleration and ϕ_0 is an arbitrary constant. Suppose the origin of the coordinate system is located at the point of levitation and that $\phi_0 = 0$. Total force derived from the total potential energy 3.19 is given by

$$\boldsymbol{F}_{\mathrm{T}} = \boldsymbol{F} - mg\mathbf{z_0}, \tag{3.20}$$

where $\mathbf{z_0}$ is unitary vector along z-axis. The Hessian matrix does not change when gravity is taken into account.

If the object is freely floating in air, the total force (3.20) is zero. The goal is to levitate as massive objects as possible, which leads to the maximization of the magnetic force along z-axis. Stable levitation also requires three-dimensional well of potential energy which should be as steep as possible.

The noted goals state the objective function to be optimized: force fighting gravity, and stability. This leads to multiobjective optimization. Force maximization is a straightforward goal. The stability, in contrast, means the maximization of the minimal eigenvalue of the Hessian matrix, which is equivalent to the convexity maximization of a quadratic potential well in three dimensions. The optimization should also properly be constrained since the magnetic force can be made as large as desired by boosting the magnitude of electric currents flowing in the design region. A natural constraint in that respect is the maximum feasible power lost by the current flowing in the supporting material.

The final optimization problem reads

$$\begin{aligned} \max_{\boldsymbol{J}} \quad & \left\{F_z, \lambda^{\min}\right\} & (3.21)\\ \text{s.t.} \quad & P_{\text{lost}} = P_{\text{lost}}^{\max}, & (3.22)\\ & F_x = F_y = 0, & (3.23) \end{aligned}$$

where $\boldsymbol{J}$ is current density (optimization variable) and $\lambda^{\min}$ is the minimal eigenvalue of the Hessian matrix introduced in (3.3). As mentioned in chapter 2, levitation of a permanent magnetic dipole is not of interest. Assuming therefore a levitation of a small polarizable body of isotropic magnetic polarizability $\alpha < 0$, the optimization problem is equivalent to

$$\begin{aligned} \max_{\boldsymbol{J}} \quad & \left\{-\Gamma_z, \tilde{\lambda}^{\min}\right\} & (3.24)\\ \text{s.t.} \quad & P_{\text{lost}} = P_{\text{lost}}^{\max}, & (3.25)\\ & \Gamma_x = \Gamma_y = 0, & (3.26) \end{aligned}$$

where $\tilde{\lambda}^{\min}$ is the smallest eigenvalue of matrix $\boldsymbol{\Xi}$. Since all quantities, $\boldsymbol{F}, \lambda^{\min}$ are proportional to $\boldsymbol{\Gamma}, \tilde{\lambda}^{\min}$, the optimal solution is the only one for all objects with different suitable properties, this evidence is also valid to the problem of confinement.

3.2 Confinement

The phenomenon of confinement is only important for microscopic particles, for which the gravity force is negligible compared to thermal excitation. The goal of a magnetic trap is to design a potential well with the highest possible temperature of particles that can be trapped. The optimization goals are therefore the steepness of the potential well which is assessed by the Hessian matrix and its eigenvalues and, as mentioned earlier in chapter 2, a highest possible bias field to avoid spin-flip Majorana transitions which will lead to the escape of particles from the trap. High bias field also increases the precession frequency, which is favorable, keeping in mind the assumption that the vibrational frequency must be small compared to the frequency of precession.

Similarly to levitation, the fundamental bounds on the performance of the magnetic trap are found by multiobjective optimization with two objective functions: bias field and convexity. Choosing the squared magnitude of the bias field, the optimization problem reads

$$\max_{\boldsymbol{J}} \quad \left\{\Phi, \lambda^{\min}\right\} \tag{3.27}$$

$$\text{s.t.} \quad P_{\text{lost}} = P_{\text{lost}}^{\max}, \tag{3.28}$$

$$F_x = F_y = F_z = 0. \tag{3.29}$$

Since all force components are zero, the properties of the potential energy Hessian matrix are solely dependent on matrix $\boldsymbol{\Xi}$, for both the induced magnetic dipole (3.15) and the permanent one (3.18). Then for both types of dipole optimization can therefore be rewritten as

$$\max_{\boldsymbol{J}} \quad \left\{\Phi, \tilde{\lambda}^{\min}\right\} \tag{3.30}$$

$$\text{s.t.} \quad P_{\text{lost}} = P_{\text{lost}}^{\max}, \tag{3.31}$$

$$\Gamma_x = \Gamma_y = \Gamma_z = 0. \tag{3.32}$$

The algorithms used to find the physical bounds are discussed later in section 4.3.

To illustrate the physical content of the aforementioned optimization problems, figure 3.1 shows the potential profile of two classical designs of magnetic traps, namely, the quadrupole trap, see figure 3.2a, and the Ioffe-Pritchard trap, see figure 3.2b. Their parameters[2] are taken from [9].

First of all, figure 3.1 indicates, that the quadratic approximation of the squared magnetic field magnitude in the center of the trap is sufficient for a precise description. Figure 3.1 also shows that the designs differ considerably in the two most important parameters, which are the magnetic field magnitude in the center of the trap (non-zero magnetic field is needed to avoid spin-flips) and convexity, i.e. the ability of the trap to localize the trapped objects. If the eigenvalues are higher, the confined objects are better localized. It can be seen that the quadrupole trap exhibits higher overall convexity but insufficient polarizing magnetic field. Ioffe-Pritchard trap offers great convexity in the xy-plane, non-zero polarizing field, but fails to localize the particle along z-direction.

Both realized traps can clearly be optimized for better performance, which is the role of mathematical formulation (3.30)–(3.32), which aims to equalize convexity in all directions, make it as high as possible and also to put this metric in mutual trade-off with maximum polarizing field in the center of the trap.

---

[2] Ioffe-Pritchard trap with loop radius 1 cm, distance from origin 1.25 cm, wires distance from origin 1.41 cm, current in loops 300 A and wires 10^4 A. Parameters of quadrupole trap are written in section 5.2.

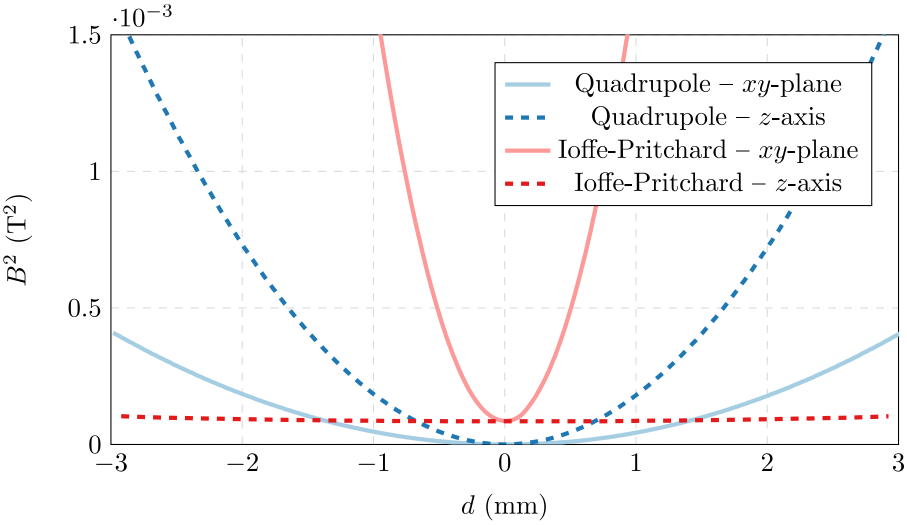

Figure 3.1: Potential well of Quadrupole and Ioffe-Pritchard trap [9] plotted in cuts.

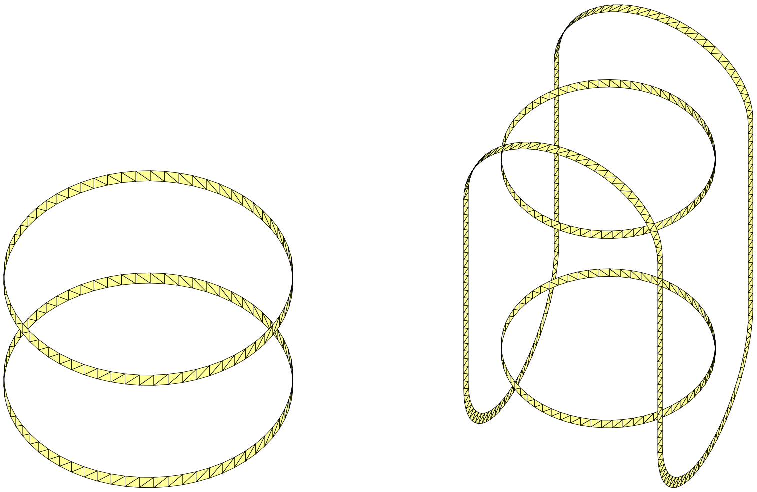

(a) : Quadrupole trap.

(b) : Ioffe-Pritchard trap.

Figure 3.2: Examples of magnetic traps.

Chapter 4

Computational Tools

This chapter introduces the basic tools of mathematical physics used in the thesis, starting from the matrix formulation of the magnetic field and its derivatives through the expansion of the current density into a set of basis functions and use of method of moments (MoM). Subsequent section introduces field-integral description of electromagnetic field, electric field integral equation (EFIE), which is used to obtain entire-domain basis functions suitable to represent stationary (zero-divergence) current density, as well as to evaluate currents on metallic objects excited by sources under quasi-static conditions. Finally, basics of quadratically constrained quadratic program (QCQP) are shown and used to formulate the fundamental bounds of magnetic levitation and confinement.

4.1 B-field Operators

Under quasistatic conditions, the magnetic field excited by a stationary current density $\boldsymbol{J}$ is given by Biot-Savart's formula [12, section 10.2], [22, section 5.3],

$$\boldsymbol{B}(\boldsymbol{r}) = \frac{\mu_0}{4\pi} \int \boldsymbol{J}(\boldsymbol{r}') \times \frac{\boldsymbol{R}(\boldsymbol{r},\boldsymbol{r}')}{|\boldsymbol{R}(\boldsymbol{r},\boldsymbol{r}')|^3} \, \mathrm{d}V', \quad \boldsymbol{R}(\boldsymbol{r},\boldsymbol{r}') = \boldsymbol{r} - \boldsymbol{r}'. \tag{4.1}$$

Assuming that the current density is expanded in a set of appropriate basis functions as

$$\boldsymbol{J}(\boldsymbol{r}') \approx \sum_{n=1}^{N} I_n \boldsymbol{\psi}_n(\boldsymbol{r}'), \tag{4.2}$$

then, the Biot-Savart's formula (4.1) reads

$$\boldsymbol{B} \approx \mathbf{B}\mathbf{I}, \quad \mathbf{B} \in \mathbb{R}^{3\times N}, \tag{4.3}$$

where the current expansion coefficients have been collected into a column vector $\mathbf{I}$, and where columns of matrix $\mathbf{B}$ are given by

$$\mathbf{B}_n = \frac{\mu_0}{4\pi} \int\limits_{V_n} \boldsymbol{\psi}_n(\boldsymbol{r}') \times \boldsymbol{g}(\boldsymbol{r}, \boldsymbol{r}') \, \mathrm{d}V' \tag{4.4}$$

with substitution

$$\boldsymbol{g}(\boldsymbol{r}, \boldsymbol{r}') = \frac{\boldsymbol{R}(\boldsymbol{r}, \boldsymbol{r}')}{|\boldsymbol{R}(\boldsymbol{r}, \boldsymbol{r}')|^3}. \tag{4.5}$$

An important merit of this matrix formulation is that matrix $\mathbf{B}$ only depends on a given distribution of basis functions $\boldsymbol{\psi}_n(\boldsymbol{r})$ and on the observation point $\boldsymbol{r}$. The evaluation of magnetic field at that point is then reduced to a matrix multiplication (4.3) allowing for fast evaluation for arbitrary current distribution described by current vector $\mathbf{I}$.

Apart from the magnetic field also its first and second spatial derivatives (3.5) and (3.6) are needed to be evaluated. These can be easily obtained from the Biot-Savart's formula (4.1). Following the procedure analogous to (4.1)–(4.5), it is possible to write

$$\frac{\partial \boldsymbol{B}}{\partial i} \approx \mathbf{B}_{,i}\mathbf{I}, \quad \mathbf{B}_{,i} \in \mathbb{R}^{3\times N} \tag{4.6}$$

$$\frac{\partial^2 \boldsymbol{B}}{\partial j \partial i} \approx \mathbf{B}_{,ij}\mathbf{I}, \quad \mathbf{B}_{,ij} \in \mathbb{R}^{3\times N} \tag{4.7}$$

where columns of matrices $\mathbf{B}_{,i}$ and $\mathbf{B}_{,ij}$ read

$$\mathbf{B}_{n,i} = \frac{\mu_0}{4\pi} \int\limits_{V_n} \boldsymbol{\psi}_n(\boldsymbol{r}') \times \frac{\partial \boldsymbol{g}(\boldsymbol{r}, \boldsymbol{r}')}{\partial i} \, \mathrm{d}V', \tag{4.8}$$

$$\mathbf{B}_{n,ij} = \frac{\mu_0}{4\pi} \int\limits_{V_n} \boldsymbol{\psi}_n(\boldsymbol{r}') \times \frac{\partial^2 \boldsymbol{g}(\boldsymbol{r}, \boldsymbol{r}')}{\partial j \partial i} \, \mathrm{d}V'. \tag{4.9}$$

Practical implementation of integrals used in (4.4), (4.8), (4.9) involves a numerical quadrature and is detailed in appendix A.

The derived matrix operators $\mathbf{B}, \mathbf{B}_{,i}, \mathbf{B}_{,ij}$ are in the subsequent text used to express squared magnitude of magnetic field (3.4), its gradient (3.5) and Hessian matrix (3.6), they can be written elementwise as quadratic forms of current vector $\mathbf{I}$

$$\Phi \approx \mathbf{I}^{\mathrm{H}} \boldsymbol{\Phi} \mathbf{I}, \tag{4.10}$$

$$\Gamma_i \approx \mathbf{I}^{\mathrm{H}} \boldsymbol{\Gamma}_i \mathbf{I}, \tag{4.11}$$

$$\Xi_{ij} \approx \mathbf{I}^{\mathrm{H}} \boldsymbol{\Xi}_{ij} \mathbf{I}, \tag{4.12}$$

where

$$\boldsymbol{\Phi} = \mathbf{B}^{\mathrm{T}}\mathbf{B}, \tag{4.13}$$

$$\boldsymbol{\Gamma}_i = -\left(\mathbf{B}_{,i}^{\mathrm{T}}\mathbf{B} + \mathbf{B}^{\mathrm{T}}\mathbf{B}_{,i}\right), \tag{4.14}$$

$$\boldsymbol{\Xi}_{ij} = \left(\mathbf{B}_{,ij}^{\mathrm{T}}\mathbf{B} + \mathbf{B}^{\mathrm{T}}\mathbf{B}_{,ij} + \mathbf{B}_{,j}^{\mathrm{T}}\mathbf{B}_{,i} + \mathbf{B}_{,i}^{\mathrm{T}}\mathbf{B}_{,j}\right), \tag{4.15}$$

are symmetric matrices from their definition.

4.2 Electric Field Integral Equation and Method of Moments

This section focuses on the application of MoM on EFIE using an expansion of current density to basis functions[1] partially discussed in appendix A. One of the important aims is also to create zero-divergence entire-domain basis functions as specific linear combinations of basis functions in order to form an expansion basis suitable to describe quasi-static electromagnetic problems[2].

MoM application to EFIE recasts an electromagnetic problem containing electric conductors and electric sources into a linear equations system [24]

$$(\mathbf{Z}_\rho + \mathbf{Z}_0)\,\mathbf{I} = \mathbf{V}, \tag{4.16}$$

$$\mathbf{Z}_\rho = \mathbf{R}_\rho + \mathrm{i}\mathbf{X}_\rho, \tag{4.17}$$

$$\mathbf{Z}_0 = \mathbf{R}_0 + \mathrm{i}\mathbf{X}_0 \tag{4.18}$$

where $\mathbf{Z}_\rho$ denotes material part of impedance matrix with real part $\mathbf{R}_\rho$ corresponding to ohmic losses and imaginary part $\mathbf{X}_\rho$ related to reactance, and where $\mathbf{Z}_0$ denotes vacuum part of impedance matrix, with real part $\mathbf{R}_0$ corresponding to radiation and imaginary part $\mathbf{X}_0$ to reactance. Vector $\mathbf{V}$ represents electric sources. Element-wise, the impedance matrix and excitation vector reads [24]

$$z^\rho_{mn}(k) = Z_\mathrm{m}(k) \int\limits_V \boldsymbol{\psi}_m(\boldsymbol{r}) \cdot \boldsymbol{\psi}_n(\boldsymbol{r}) \;\mathrm{d}V, \tag{4.19}$$

$$\begin{aligned} z^0_{mn}(k) =& \mathrm{i}k\sqrt{\frac{\mu_0}{\varepsilon_0}} \int\limits_V \int\limits_V \Big[\boldsymbol{\psi}_m(\boldsymbol{r}) \cdot \boldsymbol{\psi}_n(\boldsymbol{r}') + \\ & - \frac{1}{k^2}\nabla \cdot \boldsymbol{\psi}_m(\boldsymbol{r}) \nabla' \cdot \boldsymbol{\psi}_n(\boldsymbol{r}')\Big] G(\boldsymbol{r}, \boldsymbol{r}', k) \;\mathrm{d}V' \,\mathrm{d}V, \end{aligned} \tag{4.20}$$

$$v_m(k) = \int\limits_V \boldsymbol{\psi}_m(\boldsymbol{r}) \cdot \boldsymbol{E}^\mathrm{i}(\boldsymbol{r}, k) \;\mathrm{d}V. \tag{4.21}$$

with free-space wavenumber

$$k = \omega\sqrt{\varepsilon_0 \mu_0}, \tag{4.22}$$

the free-space Green's function

$$G(\boldsymbol{r}, \boldsymbol{r}', k) = \frac{\mathrm{e}^{-\mathrm{i}k|\boldsymbol{r}-\boldsymbol{r}'|}}{|\boldsymbol{r}-\boldsymbol{r}'|} \tag{4.23}$$

---

[1] RWG [23] basis functions are defined over triangular mesh and are used to expand surface current density, which is solely used in all problems in the thesis.

[2] In the subsequent text, time-harmonic steady state under time convention $\mathrm{e}^{-\mathrm{i}\omega t}$ is assumed with ω being angular velocity.

impressed electric field $\boldsymbol{E}^{\mathrm{i}}$ and with

$$Z_{\mathrm{m}}(k) = R_{\mathrm{m}}(k) + \mathrm{i}X_{\mathrm{m}}(k) \tag{4.24}$$

being the material impedance of conductors, whose real part R_{m} denotes resistance and imaginary part X_{m} denotes reactance. Matrix $\mathbf{R}_\rho$ is positive definite (it represents losses) and impedance matrix $(\mathbf{Z}_\rho + \mathbf{Z}_0)$ is invertible. The evaluation is implemented in MATLAB® [25] as a part of Antenna Toolbox for MATLAB (AToM)[3].

The description via EFIE and RWG basis functions is primarily used in electromagnetic scattering and it cannot be directly used for quasi-static problems in its native form. A better formulation would use magneto-static integral equation for which however the open codes are not available. For that reason, the EFIE will be used in this thesis and the modifications described below will be employed to make this description stable also in quasistatic scenarios.

Application of EFIE to quasistatic problems causes problems. The major problem of EFIE and RWG is the assumption of nonzero charge density on every basis function, i.e., of nonstationary current density. This is not a major problem for the realized excited problems, the current $\mathbf{I}$ on which is evaluated by direct inversion

$$\mathbf{I} = (\mathbf{Z}_\rho + \mathbf{Z}_0)^{-1}\,\mathbf{V}. \tag{4.25}$$

There, the excitation vector $\mathbf{V}$ forces the current to behave accordingly to the real physical situation, i.e., to erase the charge density in quasi-magnetostatic scenarios. In the case of optimization, however, a proper set of basis functions has to be used, because the application of fully dynamical basis functions to quasi-static magnetic problems can result in physically nonsensical current density since no real excitation restricts its shape. Another unpleasant problem is the second term in the evaluation of the vacuum part of the impedance matrix (4.20). This second part containing the divegergence of basis functions is divided by the wavenumber k. If the wavenumber goes to zero (or is very small compared to the extent of the basis functions), which is the case of the quasi-static scenario used in this thesis, this part of the integral diverges (or at least causes numerical issues). In order to avoid this second difficulty, a nonvanishing electric size $ka > 10^{-3}$, where a is the radius of the smallest sphere circumscribing the structure, is used.

To remove this deficiency, a proper combination of RWG basis functions will be derived in subsequent section 4.2.1 forming a new basis with minimum excess charge and therefore well adapted to describe stationary currents.

---

[3] Author of the thesis is also a member of AToM development team.

4.2.1 “Loop-Star” Decomposition

The construction of a basis with minimum (ideally zero) charge density requires the knowledge of the cycle mean electric and magnetic energy, which, by description (4.16), can be defined as [26]

$$W_{\mathrm{e}} = \frac{1}{4\omega}\mathbf{I}^{\mathrm{H}}\mathbf{X}_{\mathrm{e}}\mathbf{I}, \tag{4.26}$$

$$W_{\mathrm{m}} = \frac{1}{4\omega}\mathbf{I}^{\mathrm{H}}\mathbf{X}_{\mathrm{m}}\mathbf{I}, \tag{4.27}$$

where

$$\mathbf{X}_{\mathrm{e}} = \frac{1}{2}\left(\omega\frac{\partial\mathbf{X}}{\partial\omega} - \mathbf{X}\right), \tag{4.28}$$

$$\mathbf{X}_{\mathrm{m}} = \frac{1}{2}\left(\omega\frac{\partial\mathbf{X}}{\partial\omega} + \mathbf{X}\right). \tag{4.29}$$

General current density flow can be composed of solenoidal $\boldsymbol{J}_{\mathrm{m}}$ and irrotational $\boldsymbol{J}_{\mathrm{e}}$ parts [27]

$$\boldsymbol{J} = \boldsymbol{J}_{\mathrm{m}} + \boldsymbol{J}_{\mathrm{e}}. \tag{4.30}$$

where under quasistatic conditions (vanishingly small electric size of the analyzed object), the solenoidal (loop-like) current density provides zero divergence and generates predominantly magnetic energy, while the irrotational (star-like) current density generates predominantly electric energy. Employing (4.28) and (4.29), the decomposition of current density (4.30) can approximately be achieved by eigenvalue decomposition

$$\mathbf{X}_{\mathrm{m}}\mathbf{Q} = \mathbf{X}_{\mathrm{e}}\mathbf{Q}\mathbf{D}, \tag{4.31}$$

where loop-like current densities are eigenvectors (columns in matrix $\mathbf{Q}$) with eigenvalues (elements of diagonal matrix $\mathbf{D}$) greater than one (their cycle mean magnetic energy is greater than the electric energy) and vice versa for eigenvectors representing star-like current densities. These loop-like eigenvectors will be used in this thesis as the basis for all stationary current distributions.

An example of decomposition (4.31) is shown in figure 4.1. The plot of current density clearly demonstrates the decomposition into loop-like and star-like current densities.

The decomposition (4.31) allows to define new entire domain basis functions

$$\Psi_i = \sum_n Q_{ni}\boldsymbol{\psi}_n, \;\; D_{ii} > 1 \tag{4.32}$$

suitable for the description of quasi-magnetostatic problems. In which follows, basis functions $\{\Psi_n\}$ are used instead of basis functions $\{\boldsymbol{\psi}_n\}$. The operators

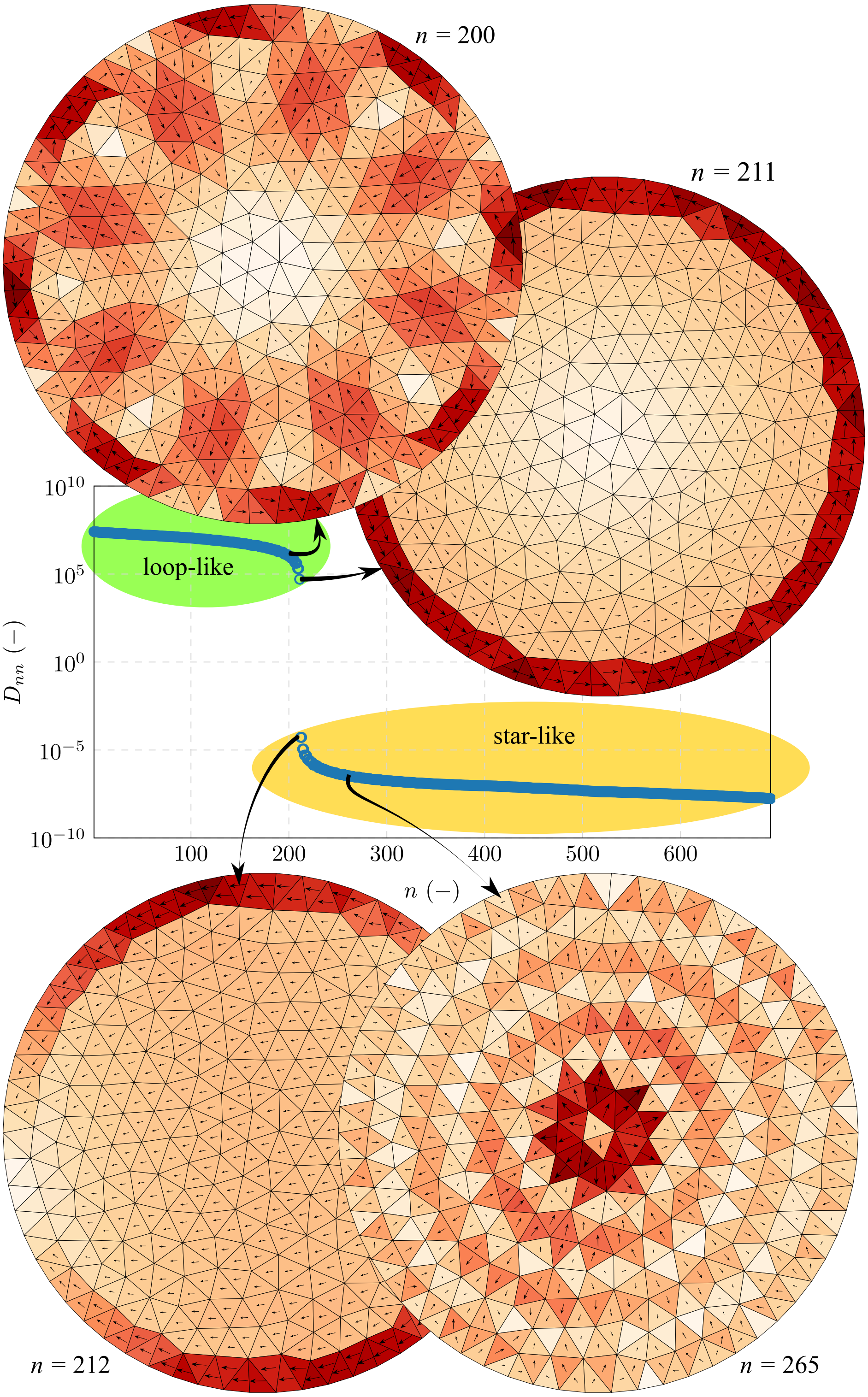

Figure 4.1: “Loop-Star” decomposition over RWG basis functions distributed on a circle which is discretized into 500 triangles. Variable n represents number of eigenvalue.

expressed in basis $\{\psi_n\}$ are transformed into new basis $\{\Psi_n\}$ by matrix $\mathbf{Q}_\mathrm{l}$ which columns are those eigenvectors of (4.31) with eigenvalues greater than one. The operators of magnetic field, its first and second derivatives in the new basis are formed as

$$\mathbf{B}_n \sim \mathbf{B}_n \mathbf{Q}_\mathrm{l}, \tag{4.33}$$

$$\mathbf{B}_{n,i} \sim \mathbf{B}_{n,i} \mathbf{Q}_\mathrm{l}, \tag{4.34}$$

$$\mathbf{B}_{n,ij} \sim \mathbf{B}_{n,ij} \mathbf{Q}_\mathrm{l}. \tag{4.35}$$

4.3 Optimization

This section introduces quadratically constrained quadratic program (QCQP), which is used to solve optimization problems leading to fundamental bounds of magnetic levitation and confinement. In these formulations, the current density vector $\mathbf{I}$ is used as an optimized variable.

Throughout this work, the following form of QCQP is considered

$$\min_{\mathbf{I}} \quad \left(\mathbf{I}^\mathrm{H}\mathbf{A}\mathbf{I} + \mathbf{I}^\mathrm{H}\mathbf{a} + \alpha\right) \tag{4.36}$$

$$\text{s.t.} \quad \mathbf{I}^\mathrm{H}\mathbf{C}_i\mathbf{I} + \mathbf{I}^\mathrm{H}\mathbf{c}_i + \gamma_i = 0; \quad \forall i = 1, \dots, m \tag{4.37}$$

where

$$\begin{aligned} &\mathbf{I}, \mathbf{a}, \mathbf{c}_i \in \mathbb{C}^{n \times 1}, \\ &\mathbf{A}, \mathbf{C}_i \in \mathbb{C}^{n \times n}, \\ &\alpha, \gamma_i \in \mathbb{R}, \\ &\mathbf{C}_1 \succ 0, \end{aligned}$$

all matrices are Hermitian and where the solution is supposed to exist. The solution is approached via duality [28, sections 12.9,16.1], [29, chapter 5] and its implementation is done in MATLAB® [25]. Matrix $\mathbf{R}_\rho$ is considered in all problems as matrix $\mathbf{C}_1$. This matrix is of full rank, it is positive definite, determines ohmic losses in the optimized structure, and provides a natural normalization of vector $\mathbf{I}$ not letting its elements to be unbounded.

In sections 3.1, 3.2, the optimization problems were introduced in general terms. The following two subsections employ the formulation of the squared magnetic field and its first and second derivatives via quadratic forms in the current density vector (4.10) – (4.12) and give explicit QCQP forms of optimization problems for magnetic levitation (3.24) – (3.26) and magnetic confinement (3.30) – (3.32).

4.3.1 Levitation

As discussed in chapter 3, the quality of the spatial distribution of the magnetic field with respect to levitation is determined by the force fighting gravity and stability, which results in Pareto-optimal set of these two objective functions [30]. The curvature of the potential (stability criterion) is however related to the eigenvalues of Hessian matrix and is therefore not a quadratic form of current vector. As presented in (3.24) – (3.26), the optimization problem does not belong to QCQP.

To overcome this difficulty, an assumption is made (and enforced by optimization constraints) that the Hessian matrix is diagonal (all off-diagonal terms are zero) and all diagonal terms are equal. Consequence of this assumption is that all eigenvalues of Hessian matrix $\tilde{\lambda}$ are equal and on top of that they matches the diagonal terms of the Hessian matrix. This requirement results in equal convexities of squared magnetic field magnitude in all directions and, importantly, to convexity described by a quadratic form of current vector. A drawback of this assumption is the loss of freedom in current vector $\mathbf{I}$ and therefore a possible shift of the optimized values towards the suboptimal region.

With the aforementioned assumption, the optimization problem for current vector $\mathbf{I}$ which is Pareto-optimal with respect to levitation (3.24) – (3.26) is rewritten as QCQP containing two objective quadratic functions and 8 quadratic constraints,

$$\max_{\mathbf{I}} \quad \mathbf{I}^{\mathrm{H}}\left[\xi \boldsymbol{\Xi}_{xx} - (1-\xi)\boldsymbol{\Gamma}_z\right]\mathbf{I}, \quad \xi \in [0,1] \tag{4.38}$$

$$\text{s.t.} \quad \mathbf{I}^{\mathrm{H}}\mathbf{R}_{\rho}\mathbf{I} - 2 * P_{\text{lost}}^{\max} = 0, \tag{4.39}$$

$$\mathbf{I}^{\mathrm{H}}\boldsymbol{\Gamma}_i\mathbf{I} = 0, \ i \in \{x, y\} \tag{4.40}$$

$$\xi \mathbf{I}^{\mathrm{H}}(\boldsymbol{\Xi}_{ii} - \boldsymbol{\Xi}_{jj})\mathbf{I} = 0, \ \forall i \neq j \tag{4.41}$$

$$\xi \mathbf{I}^{\mathrm{H}}\boldsymbol{\Xi}_{ij}\mathbf{I} = 0, \ \forall i \neq j \tag{4.42}$$

The coefficient ξ provides a linear combination of the objective functions and sweeps over Pareto-optimal sets.

The constraints on maximum lost power and on vanishing xy-components of gradient of squared magnetic field magnitude (3.25), (3.26) are directly related to quadratic constraints (4.39), (4.40). The constrains (4.41), (4.42) ensure that Hessian matrix $\boldsymbol{\Xi}$ is equal to a scalar multiple of identity matrix. The element $\boldsymbol{\Xi}_{\mathbf{xx}}$ can therefore be considered as the smallest eigenvalue of Hessian matrix $\tilde{\lambda}^{\min}$, which denotes convexity. The linear combination used as the optimized metric provides trade-off between the maximization of convexity and maximization of force in z-direction. The Pareto-optimal set is swept via coefficient ξ.

The solutions to optimization problem (4.38)–(4.42) for different coefficients ξ do not necessarily satisfy the basic condition for levitation, i.e., positive z-component of force and convexity in all directions. If coefficient ξ providing a linear combination of the objective function is close to zero, the optimization prefers maximization of force at the cost of potential curvature which might even become concave (levitation will be unstable). On the other side, if coefficient ξ is close to unity, the importance of force is diminished, which leads to high convexity but might also lead to the magnetic force being unable to compensate gravity. The appropriate range of coefficient ξ must therefore be set after the optimization process.

4.3.2 Confinement

The same assumption on Hessian matrix $\boldsymbol{\Xi}$ as in section 4.3.1 is made in the optimization problem for confinement (3.27)–(3.29) the QCQP form of which reads

$$\begin{aligned}
\max_{\mathbf{I}} \quad & \mathbf{I}^{\mathrm{H}}\left[\xi\boldsymbol{\Xi}_{xx} + (1-\xi)\boldsymbol{\Phi}\right]\mathbf{I}, \quad \xi \in [0,1] && (4.43)\\
\text{s.t.} \quad & \mathbf{I}^{\mathrm{H}}\mathbf{R}_{\rho}\mathbf{I} - 2 * P_{\text{lost}}^{\max} = 0, && (4.44)\\
& \mathbf{I}^{\mathrm{H}}\boldsymbol{\Gamma}_{i}\mathbf{I} = 0,\ \ i \in \{x,y,z\} && (4.45)\\
& \xi\mathbf{I}^{\mathrm{H}}(\boldsymbol{\Xi}_{ii} - \boldsymbol{\Xi}_{jj})\mathbf{I} = 0,\ \ \forall i \neq j && (4.46)\\
& \xi\mathbf{I}^{\mathrm{H}}\boldsymbol{\Xi}_{ij}\mathbf{I} = 0,\ \ \forall i \neq j && (4.47)\\
& \mathbf{B}_{i}\mathbf{I} = 0,\ \ i \in \{x,y\}. && (4.48)
\end{aligned}$$

where coefficient ξ again provides a linear combination of objective functions. The difference to optimization problem (4.38)–(4.42) is that instead of maximizing z-component of force, squared magnetic field magnitude is maximized. In this case, the entire force vector is zeroed via constraints (4.45).

The additional constraint (4.48), which is not taken into account in original problem (3.27)–(3.29), limits the magnetic field in the trap to point only in z-direction. This is a nonrestrictive assumption, which allows to set the direction of trapped particles polarization. The linear constraints on magnetic field (4.48) can easily be fulfilled by employing null-space of matrix $\mathbf{B}_i$. Furthermore, if x, y-components of magnetic field are zero and z-component of magnetic field is non-zero, the only way to ensure zero force in the trapping center is to use vectors from a null-space common to matrices $\mathbf{B}_{z,i}$, which is a consequence of relation (3.5). With the assumption, the optimization reads

$$\begin{aligned}
\max_{\mathbf{I}} \quad & \mathbf{I}^{\mathrm{H}} \left[\xi \mathbf{\Xi}_{xx} + (1-\xi)\mathbf{\Phi}\right] \mathbf{I}, \quad \xi \in [0,1] && (4.49)\\
\text{s.t.} \quad & \mathbf{I}^{\mathrm{H}}\mathbf{R}_\rho \mathbf{I} - 2 * P_{\mathrm{lost}}^{\mathrm{max}} = 0, && (4.50)\\
& \xi \mathbf{I}^{\mathrm{H}}(\mathbf{\Xi}_{ii} - \mathbf{\Xi}_{jj})\mathbf{I} = 0, \ \forall i \neq j && (4.51)\\
& \xi \mathbf{I}^{\mathrm{H}}\mathbf{\Xi}_{ij}\mathbf{I} = 0, \ \forall i \neq j && (4.52)\\
& \mathbf{B}_i \mathbf{I} = 0, \ i \in \{x, y\} && (4.53)\\
& \mathbf{B}_{z,i} \mathbf{I} = 0, \ i \in \{x, y, z\}. && (4.54)
\end{aligned}$$

Analogously to the optimization problem for levitation, the solutions to optimization problem (4.38)–(4.42) for different coefficients ξ do not have to always satisfy the condition for confinement: squared magnetic field magnitude convexity in all directions. It might happen that a concave potential (unstable equilibrium) is produced when coefficient ξ is close to zero. On the other side, if coefficient ξ is close to one, the magnetic field magnitude might tend to be zero, but a nonzero magnetic field is not a strict condition for confinement. Its presence is only desired to avoid the loss of particles due to spin-flip effects and to justify the adiabatic approximation.

4.3.3 Subspace Reduction

The optimization problems (4.38)–(4.42), (4.49)–(4.54) consist of matrices representing cycle mean lost power $\mathbf{R}_\rho$, squared magnetic field, its first and second derivatives. Furthermore, except of matrix $\mathbf{R}_\rho$, these matrices are composed solely of magnetic field and its first and second derivatives, which induces that matrices can be at maximum formed by 30 independent rows[4]. Thanks the restrictions (3.7)–(3.9), which contains 7 independent equations, the maximal number of independent rows is further reduced to 23 and this subspace can be advantageously treated as a new set of basis function (specific linear combinations of basis functions $\{\mathbf{\Psi}_n\}$) to which all operators might be mapped. The new set of basis functions is accomplished by generalized eigenvalue decomposition

$$\mathbf{\Omega}^{\mathrm{T}}\mathbf{\Omega}\mathbf{I} = \lambda \mathbf{R}_\rho \mathbf{I}, \tag{4.55}$$

---

[4] Three vectors are given by B-field operators (3 components), 9 by first derivatives (3 components, 3 derivatives) and 18 by second derivatives (3 components, 6 different second derivatives).

where

$$\boldsymbol{\Omega} = \begin{pmatrix} \mathbf{B} \\ \mathbf{B}_{,x} \\ \mathbf{B}_{,y} \\ \mathbf{B}_{,z} \\ \mathbf{B}_{,xx} \\ \vdots \\ \mathbf{B}_{,ij} \\ \vdots \\ \mathbf{B}_{,zz} \end{pmatrix}, \quad \boldsymbol{\Omega} \in \mathbb{R}^{30\times N}. \tag{4.56}$$

Eigenvectors corresponding to nonzero eigenvalues given by the generalized eigenvalue problem (4.55) generate the subspace with the basis vectors important to magnetic potential energy operators. As mentioned earlier in chapter 2, ohmic losses constraints the optimal current density, so the desired basis is orthogonal according to the cycle mean ohmic losses matrix $\mathbf{R}_\rho$.

Notice, that the subspace dimension has to be lower or equal[5] to 23. The evidence simplifies further computation and immensely decreases optimization complexity, it allows to reduce the basis solely to a few independent vectors. For the particular case of a spherical shell and trapping center corresponding to its center, the set current density profiles within this subset are thoroughly analyzed, discussed and its properties are highlighted in appendix B.

---

[5] Since all basis functions representing current density are solenoidal, see section 4.2.1, the rank of matrix $\boldsymbol{\Omega}$ is in fact 15 and not 23.

Chapter 5

Results

This chapter summarises all outcomes of the thesis and presents the results in two sections: levitation and confinement. The study of magnetic confinement further opens new interesting questions and topics for further study.

5.1 Magnetic Levitation

The problem of magnetic levitation is introduced in section 3.1 with appropriate mathematical and physical description. This chapter shows some levitator realizations and compares them to the physical bounds, which are determined through optimization (4.38)–(4.42) introduced in section 4.3.1.

For levitation, only planar structures are considered, although solenoids are practically used [13, 14]. This simplification is not overly restrictive and it leads to unimportant qualitative changes.

The degrees of freedom in the design of levitator: the shape of the bounding box, absolute size, material, current distribution, current amplitude are many. To compare different designs and to apprise the levitator geometry performance, a normalization

$$\frac{a^2 R_\mathrm{s}}{\mu_0^2 P_\mathrm{lost}} B^2 = \frac{a^2 R_\mathrm{s}}{\mu_0^2 P_\mathrm{lost}} \Phi \quad (-) \tag{5.1}$$

is applied, where a is a radius of the smallest sphere circumscribing the current support and R_s is the real part of surface impedance[1] Z_s. This normalization removes the dependence on the used material and on absolute dimensions.

---

[1] All evaluations were performed using surface resistance $R_\mathrm{s} = 0.01\,\Omega$.

Normalized gradient[2] (3.5) of squared magnitude of the magnetic field

$$\frac{-a^3 R_\mathrm{s}}{\mu_0^2 P_\mathrm{lost}} \boldsymbol{\Gamma} \quad (-) \tag{5.2}$$

and normalized eigenvalues of Hessian matrix (3.6)

$$\frac{a^4 R_\mathrm{s}}{\mu_0^2 P_\mathrm{lost}} \tilde{\lambda} \quad (-) \tag{5.3}$$

are used as well.

The normalization allows to compare different structures from different materials, leaving geometry to be the main cause of varying performance. For brevity, the normalized squared magnitude of the magnetic field is in what follows referenced as potential energy, normalized gradient as force, and normalized eigenvalues of Hessian matrix as convexity. It is however important to remind that the depicted quantities are only proportional to potential energy, force, and convexity via positive factors (dependent on the levitated object), which brings no qualitative changes but may alter the depicted values.

A simple levitator can be composed of four strong permanent magnets centered at the vertices of a square [31]. In this thesis, the four permanent magnets are replaced by four conducting loops carrying a homogeneous current density, see figure 5.1a. In this configuration (loop radius 1.1 cm, distance of the loop's centers from the origin equal to 1.21 cm, radius of the smallest circumscribing sphere $a = 2.31$ cm), optimal point for stable levitation is only achieved at height $0.8a$ above the plane of the loops, with z-component of the force and convexity noted in table 5.1.

To assess the performance of the realized levitator, it is necessary to compare it with the physical bound. In section 4.3.1, multi-objective optimization for levitation (4.38)–(4.42) was introduced. A disc centered in the xy-plane and discretized in 500 triangles is used as the support for optimal current density giving the fundamental bound. Although, the optimization is introduced as multi-objective it only results in one point for all coefficient $0 < \xi \leq 1$, the objective functions, force and convexity, are not in contradiction, which rises questions to be focused on during further study. Otherwise, for $\xi = 0$, the optimization maximizes only force without any restrictions to Hessian matrix, which causes that the resulting minimal eigenvalue $\tilde{\lambda}^\mathrm{min}$ is negative and levitation is unstable. The optimal current density is shown in figure 5.1b and the performance is shown in the first row of table 5.1.

Since the optimal current density is known, one can also try to realize it. Figure 5.1b suggests that the optimal current density in essence consists of

---

[2] Keep in mind that force is proportional to minus gradient (3.1).

two loops of currents flowing in opposite directions. The task is therefore to find their appropriate radius and the ratio of currents in the inner and outer loop $I_{\mathrm{in}}/I_{\mathrm{out}}$. An attempt to do so is shown in figure 5.1c. If simple loops are replaced by cylindrical coils, this configuration is referred to as “Bitter magnet” [14]. With inner radius $0.25a$, the stable levitation at point $0.8a$ above the plain is achieved with ratio $I_{\mathrm{in}}/I_{\mathrm{out}} = 0.78$. For this configuration, the values of the force along z-direction at the point of levitation and convexity (5.3) are also noted in table 5.1.

Table 5.1: Performance in force along z-direction and convexity at the point of levitation, depicted for various domains.

	$\frac{-a^3 R_{\mathrm{s}}}{\mu_0^2 P_{\mathrm{lost}}}\Gamma_z$ $(-)$	$\frac{a^4 R_{\mathrm{s}}}{\mu_0^2 P_{\mathrm{lost}}}\tilde{\lambda}^{\mathrm{min}}$ $(-)$
fundamental bound	$6.52 \cdot 10^{-3}$	$4.07 \cdot 10^{-3}$
coaxial configuration	$2.56 \cdot 10^{-3}$	$1.49 \cdot 10^{-3}$
4-loop configuration	$4.30 \cdot 10^{-4}$	$2.65 \cdot 10^{-4}$

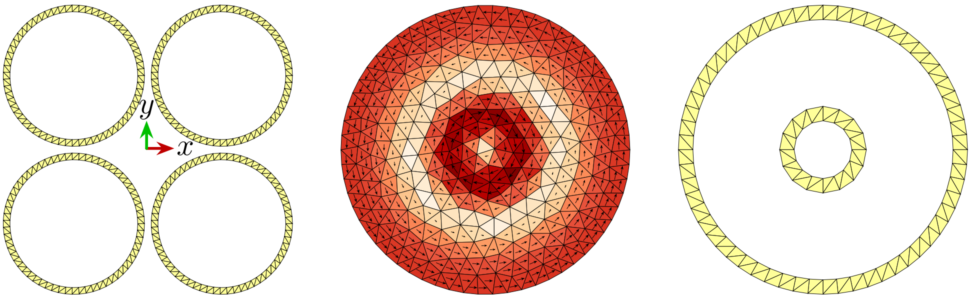

(a) : Four-loops configuration with all currents flowing in the same direction.

(b) : Optimal current density on a disc.

(c) : An attempt to mimic optimal current density with a coaxial configuration of loops. The excited currents flows in opposite directions in different loops.

Figure 5.1: Examples of levitators and optimal current density. The optimal point for levitation is placed at the axis of the system at height $0.8a$ above plane of the current density.

The conclusion is that the inspiration of the optimal current density is useful and the coaxial configuration provides almost six times better performance in both criteria than the four-loop configuration. As suggested by the performance of the optimal current, there is, however, still room for improvement.

Potential energies along the coordinate axes generated by the realizations from figures 5.1a, 5.1c and by the optimal current density from figure 5.1b are compared in figure 5.2. Notice that the force corresponds to the steepness of potential energy and the stability of levitation is judged by the convexity. The point of stable levitation is denoted by the black circles in figure 5.2 ($d/a = 0$) and parameter d/a denotes the normalized distance from the point of levitation.

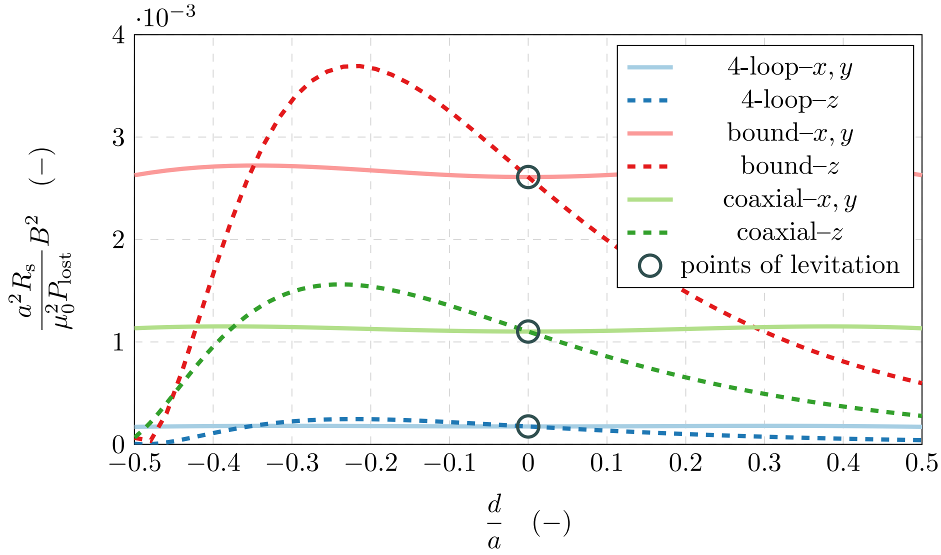

Figure 5.2: Realizations and optimal current density from figure 5.1 generates potential energy distribution plotted in cuts along axis at the point of levitation, where d/a is normalized distance from point of levitation.

Figure 5.2 also shows that the quadratic approximation of potential energy (2.2) is sufficient only near the point of levitation. This observation is detailed in figure 5.3 which shows the true potential and its quadratic approximation for the case of fundamental bound. It can be observed that the local approximation introduced in chapter 2 is only applicable when the levitating object is much smaller than the important space changes of the magnetic field. The figure 5.3 suggests that in this particular scenario, the optimal current density will only have its denoted performance for levitating objects not exceeding $0.1a$ in any direction, or in another words, for objects more than ten times smaller than the radius of the disc supporting the current.

5.2 Magnetic Confinement

This chapter presents common designs of magnetic traps and compares their performance with the corresponding fundamental bound, which was introduced in section 3.2 and mathematically formulated in section 4.3.2.

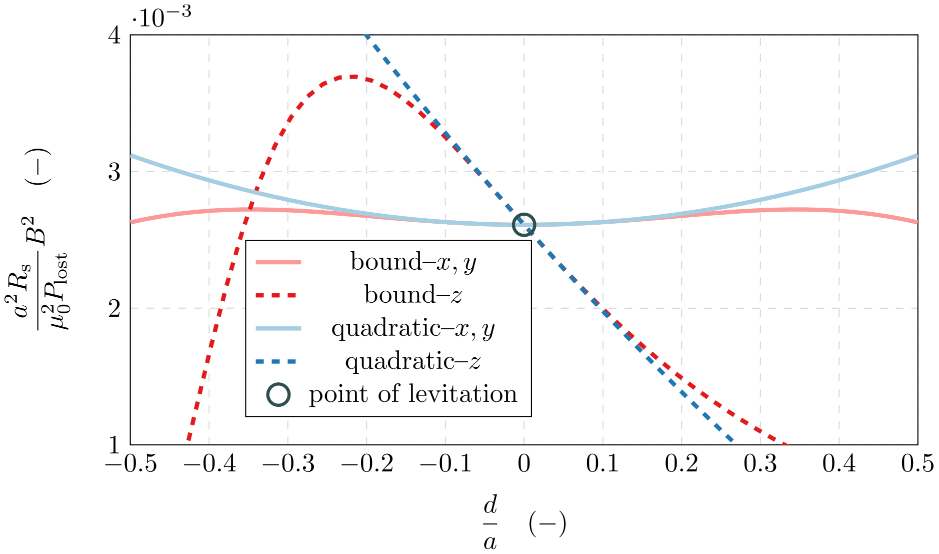

Figure 5.3: Potential energy distribution generated by optimal current in comparison to its quadratic approximation at the point of levitation plotted in cuts along axes.

Similarly to magnetic levitation, the normalization to the squared magnitude of magnetic field (3.4) and its Hessian matrix (3.6) eigenvalues are set as

$$\frac{\rho^2 R_s}{\mu_0^2 P_{\mathrm{lost}}} B^2 \quad (-), \tag{5.4}$$

$$\frac{\rho^4 R_s}{\mu_0^2 P_{\mathrm{lost}}} \tilde{\lambda} \quad (-). \tag{5.5}$$

The normalization to the gradient of the squared magnetic field magnitude is not introduced, since in magnetic levitation problems, the force at the trapping point is enforced to be zero. In contrast to magnetic levitation, the normalization by the radius of the smallest circumscribing sphere a is replaced by the radius of the largest inscribed sphere ρ centred at the trapping point since magnetic traps are typically closed structures. Similarly to the case of levitation, the normalized squared magnitude of the magnetic field (5.4) is in what follows referenced as the confinement potential and its normalized eigenvalues of Hessian matrix as convexity.

5.2.1 Common Designs of Magnetic Traps

The known designs of magnetic traps can be divided into two main groups. The first group, which includes quadrupole trap and hexapole trap as major representatives, operates with zero bias field and these traps do not actively avoid particle loss due to spin-flip Majorana transitions [9, 19]. The second group, which includes the baseball trap and Ioffe-Pritchard trap as major representatives, in contrast, avoids particle loss by operating with non-zero bias magnetic field. Performance of both kinds of traps is studied in detail in subsequent sections and is later compared to fundamental bounds.

Baseball Trap

Baseball trap is a magnetic trap with a nonzero bias magnetic field in the trapping center. The shape is inspired by the seam on a baseball ball and it is one of the practically used configurations [19, 32, 33].

Baseball trap is made of a parametrically shaped current path on the surface of a sphere which generates magnetic field confining particles in the center of the spherical surface [19]. The parametrization reads [34]

$$\boldsymbol{r}(t) = \begin{pmatrix} r_a \sin(2\pi t) + r_b \sin(6\pi t) \\ \\ r_a \cos(2\pi t) - r_b \cos(6\pi t) \\ \\ \sqrt{4 r_a r_b} \cos(4\pi t) \end{pmatrix}, \quad t \in [0, 1], \tag{5.6}$$

where $R = r_a + r_b$ is a constant distance from origin[3]. In [19], coefficients r_a and r_b are defined through angles with appropriate description as follows

$$r_a = R \cos^2\left(\frac{\pi}{4} - \beta\right), \tag{5.7}$$

$$r_b = R \sin^2\left(\frac{\pi}{4} - \beta\right), \tag{5.8}$$

$$\tag{5.9}$$

where

$$\beta = \frac{\pi}{2} - \alpha - \arccos\left(\frac{\cos\alpha}{\sqrt{2}}\right), \quad \alpha \in [0^\circ, 35.26^\circ]. \tag{5.10}$$

The geometry of baseball magnetic trap for angle $\alpha = 17^\circ$ and $\alpha = 27^\circ$ are shown in figure 5.4. Their confinement potential distributions are depicted in figure 5.5 and are parametrized by a relative position with respect to the trapping center $d/\rho = 0$. Only cuts along all axes are shown and feeding with delta-gap voltage source is assumed.

The performance of baseball trap for angle α in the range form 17° to 27° is also latter compared with fundamental bound in figure 5.9 showing that optimal angles α are in the range $[17^\circ, 22^\circ]$.

---

[3] Parameter r_b has different values for several ball seams: $0.28R$ baseball, $0.30R$ softball, $0.20R$ tennis ball and $0.38R$ basketball [34].

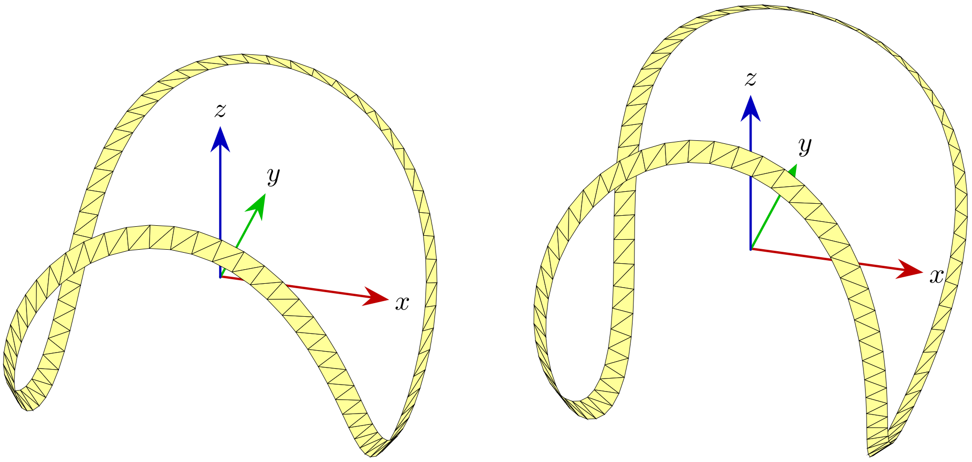

(a) : $\alpha = 17°$.

(b) : $\alpha = 22°$.

Figure 5.4: Examples of baseball magnetic traps.

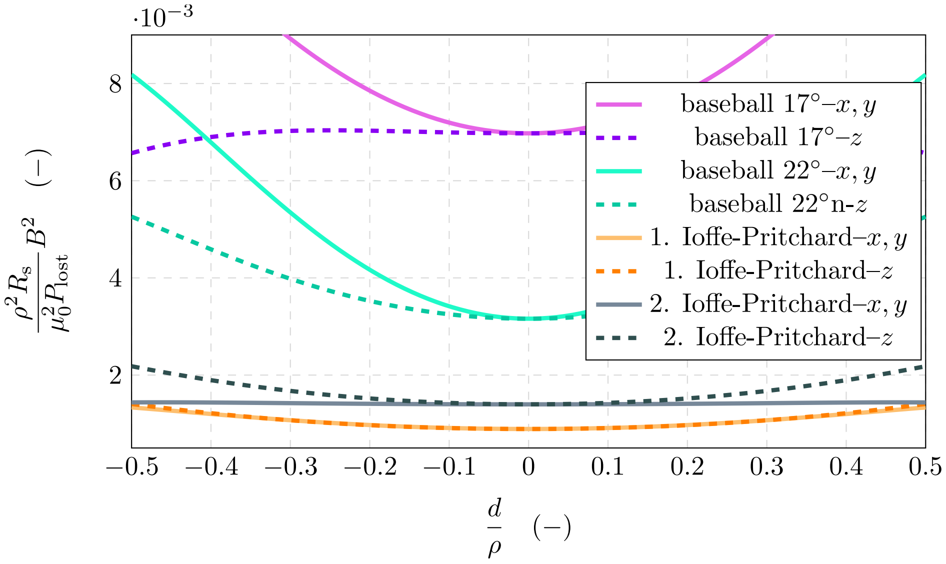

Figure 5.5: Potential wells realized by baseball and Ioffe-Pritchard traps which offer non-zero bias magnetic field in the trapping centre $d/\rho = 0$. Confinement potentials are plotted in cuts along all axes.

Ioffe-Pritchard Trap

Ioffe-Pritchard trap is another example of a practically used magnetic trap with a nonzero bias magnetic field in the trapping center. Its design is introduced in [9, 18, 19] and consists of two coaxial loops and four parallel wires passing through them. In this work, this design is slightly modified by connecting the four wires into a single connected strip, see figure 5.6a and figure 5.6b, which allows for an excitation by solely three delta-gap sources. The performance of three Ioffe-Pritchard trap configurations:

1. Loops with radius 1 cm positioned at height ±1 cm and wires distance[4] from z-axis 1 cm, whose proportions are shown in figure 5.6a. Loops are excited in same direction with current 100 A. The current flowing in parallel wires equals to 123 A. This configuration achieves the highest value of normalized hessian matrix eigenvalue among the mentioned Ioffe-Pritchard traps.

2. The geometrical proportions are same as in the previous design, the only difference being that parallel wires carry current of 70 A. This configuration achieves the highest value of normalized squared magnitude of magnetic field among the mentioned Ioffe-Pritchard traps.

3. Loops with radius 1 cm positioned at height ±1.25 cm and wires distance from z-axis equals 1 cm. The proportions are shown in figure 5.6b. Loops and parallel wires carry current of 100 A. This configuration is proposed by Bergeman in [19].

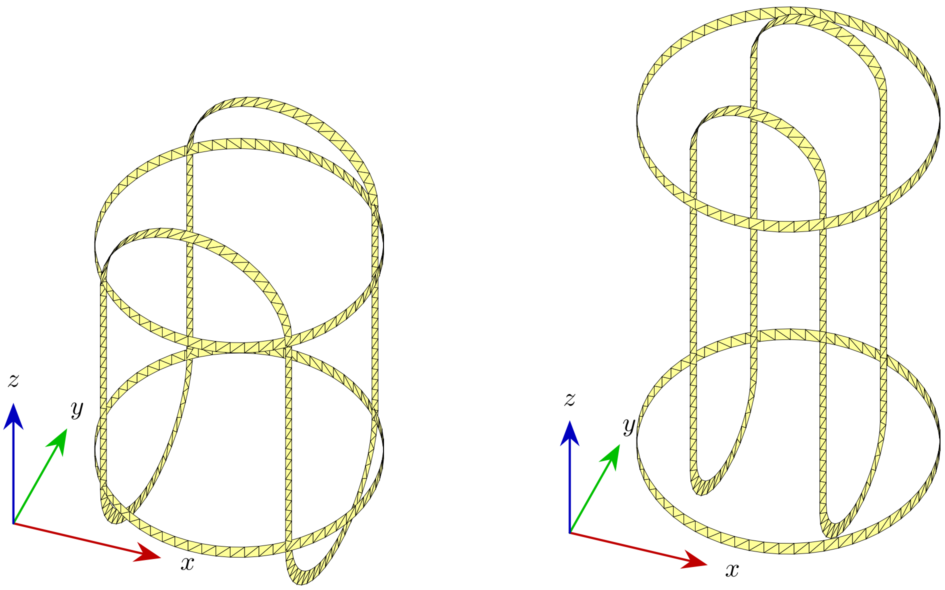

(a) : Loops with radius 1.5 cm positioned at height ±1 cm and wires distance from z-axis 1 cm.

(b) : Loop with radius 1.5 cm positioned at height ±1.25 cm and wires distance from z-axis 1 cm.

Figure 5.6: Two assessed designs of Ioffe-Pritchard traps.

are shown in figures 5.5, 5.9. Figure 5.5 shows confinement potential in cuts along all axes, while figure 5.9 focuses on the performance comparison of baseball traps and fundamental bounds.

---

[4] Vertical wires intersects with loops, which might cause problem in their physical realizations, not in the numerical simulation where no conducting contact is made.

Magnetic Traps with Zero Bias Field

Although chapter 2 introduced the assumption of strong enough magnetic field in the trapping center to allow for adiabatic approximation and to avoid spin-flip Majorana transitions [9,19], the realizations of magnetic traps with zero bias field can be found in the literature and their performance is therefore also discussed here. Two representatives are:

- Quadrupole trap proposed in [9,19] which consists of two coaxial loops with equivalent radius and identical currents flowing in opposite directions. Two particular designs are analyzed:
    - Quadrupole trap introduced by Ríos in [9] which is shown in figure 3.2a and discussed in section 3.2 and in figure 3.1. The radius of loops is 1 cm, distance from origin is 1.25 cm and current flowing in the loops equals 3000 A.
    - Quadrupole trap introduced by Bergeman in [19] which has loops of radius 1 cm, distance from origin 0.62673 cm and operates with current 100 A.

  Spatial distribution of the confinement potential generated by these two quadrupole traps is shown in figure 5.8.

- Hexapole trap is also introduced by Bergeman in [19] which consists of three loops placed on a sphere with radius 1 cm. The central loop is accompanied by two outer loops positioned $\sqrt{2}/2$ times the sphere radius above and below the origin (trapping point). The design is shown in figure 5.7. All three loops carry the same current of 100 A. The resulting space distribution of confinement potential in cuts along all axes can be found in figure 5.8.

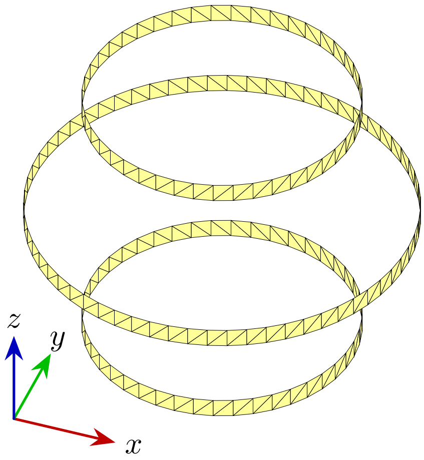

Figure 5.7: Hexapole trap.

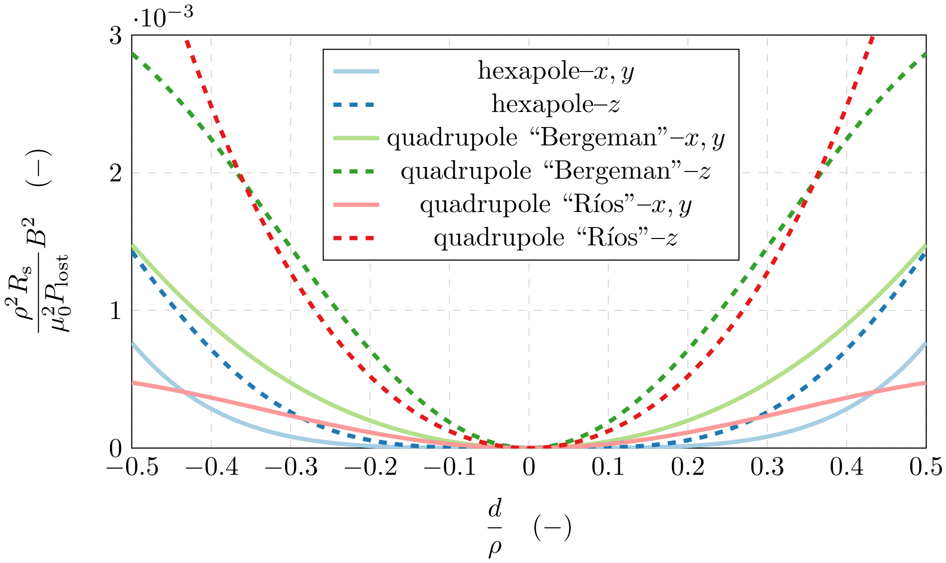

Figure 5.8: Potential wells realized by quadrupole and hexapole magnetic trap. Both traps produce zero bias magnetic field. Confinement potentials are plotted in cuts along all axes. Thanks to the rotational symmetry of quadrupole and hexapole traps around z-axis, the confinement potential plotted in cuts along x, y-axes is valid for the entire xy-plane.

Figure 5.8 shows good performance of quadrupole traps in localization of trapped particles thanks to the high convexity of the well (high normalized eigenvalues of the Hessian matrix). In the case of the hexapole trap, the eigenvalues of the Hessian matrix are equal to zero and the potential well is shaped by the spatial derivatives of the fourth order. This kind of trap does not allow for the description via second-order Taylor polynomial and is therefore out of the focus of this thesis. Figure 5.8, nevertheless, shows that the quadrupole traps outperform the hexapole trap in the localization of trapped particles.

5.2.2 Fundamental Bounds

To assess the performance of the aforementioned magnetic traps, a comparison with fundamental bounds is made. The multiobjective optimization problem resulting in the fundamental bound on magnetic confinement (4.49)–(4.54) was introduced in section 4.3.2 and it is in this section applied to three different current supporting regions: a spherical shell, a cylindrical shell and a box with the ratio of its diameter and height equal to one. In contrast to magnetic levitation, the optimization results in a populated Pareto-optimal set swept by coefficient ξ. In what follows, only those values of coefficient ξ that provides the potential wells in all directions are taken into account, see the detailed discussion in section 4.3.2 on this aspect. Fundamental bounds of confinement potential and convexity are plotted and compared to those realized by magnetic traps with non-zero bias magnetic field in figure 5.9.

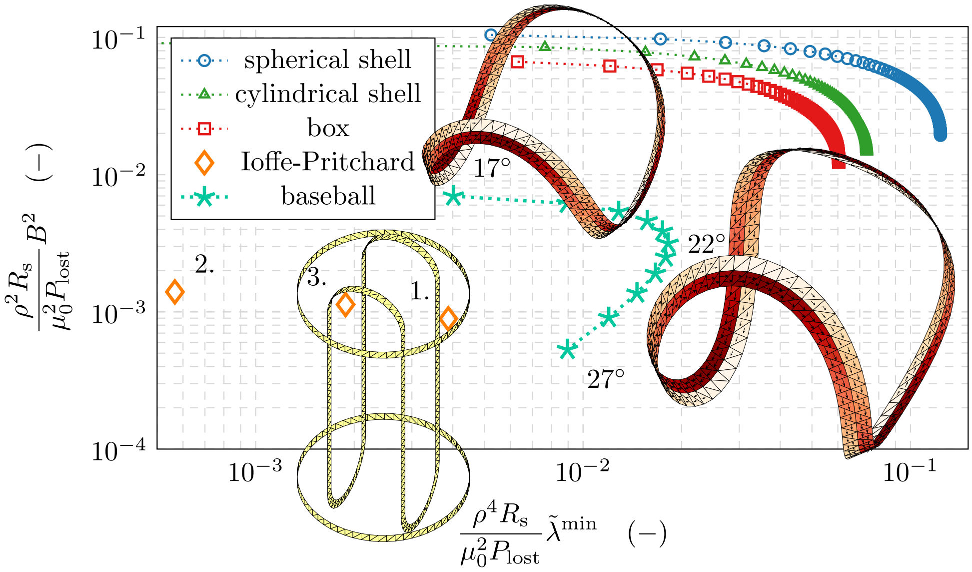

Figure 5.9: Pareto-optimal set to convexity and confinement potential in trapping center in comparison to selected practical realizations.

Figure 5.9 shows that the spherical shell dominates over other current supporting domains in both criteria. This recognition favors the use of baseball traps compared to Ioffe-Pritchard traps, which is supported by the depicted performance of both kinds of traps in the same figure.

An important difference between the potential wells produced by the optimal current density and those produced by the realized traps can also be seen from the comparison of figures 5.5, 5.8 and of figure 5.10. The optimal wells are isotropic near the trapping center, as enforced by the optimization, with only a slight anisotropy farther from it. This contrasts with the realized wells where the anisotropy is significant. The anisotropy is especially pronounced in baseball and Ioffe-Pritchad traps, greatly degrading their performance as it is the direction of the smallest curvature that dictates the localization of trapped particles.

Properties of Optimal Current Densities

Figures 5.9, 5.10 show sphere as the best geometry to achieve magnetic confinement. This section gives a detailed insight into the properties of the corresponding optimal current densities which are depicted in figure 5.11 for two points at the opposite ends of Pareto-optimal set in figure 5.9. As mentioned in section 4.3, the optimal current can be decomposed into a maximum of 15 independent current densities shown in appendix B, which

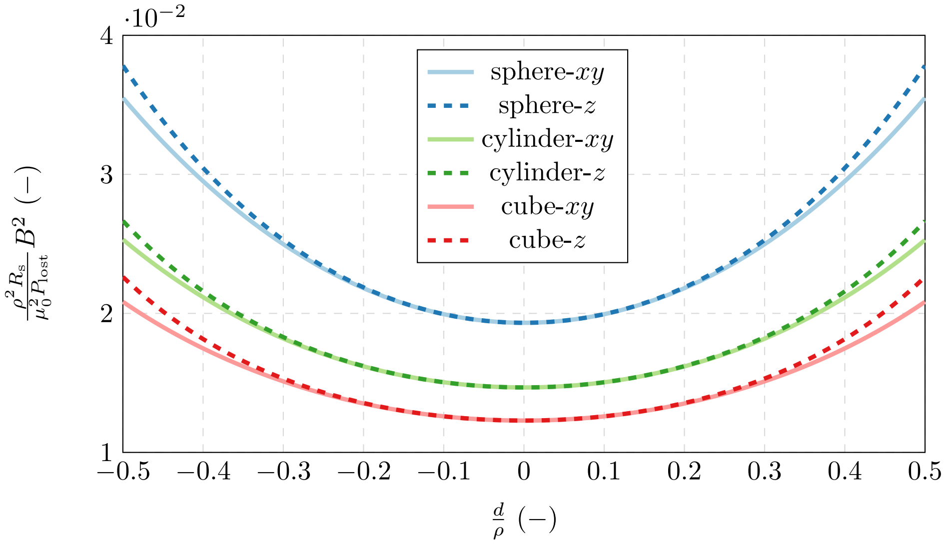

Figure 5.10: Potential wells corresponding to maximally convex Pareto-optimal points in figure 5.9 of sphere, cylinder and cube. Confinement potentials are plotted in cuts along all axes.

can be divided into three groups: one generating the magnetic field, one generating its first derivatives and one generating second derivatives of the magnetic field. The current density basis composing both optimal currents from figure 5.11 are shown in figure 5.12, giving an intuitive picture of how the optimal potential well is built. All basis currents generate a vanishing magnetic field at the trapping point (center of the sphere) except for the first, which setups the bias field along the z-axis. At the same time, all basis currents generate a vanishingly small first spatial derivative of the magnetic field z-component at the trapping center. Therefore, the two affine constraints of optimization problem (4.49)–(4.54) are satisfied independently by all basis currents. A linear combination of the basis currents is then used to form curvature of the potential well and provide trade-off between the bias field and curvature.

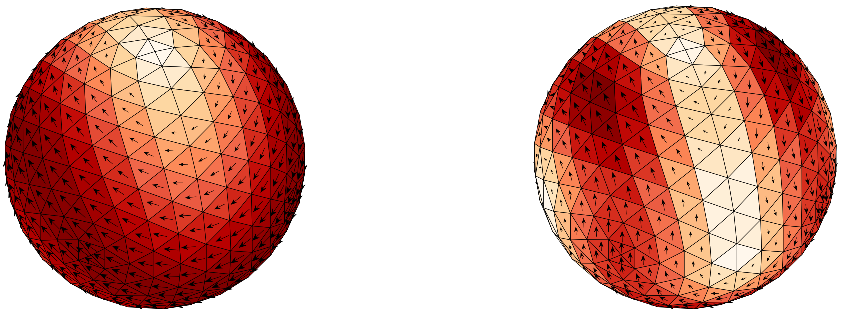

(a) : Point with low normalized convexity and high bias field.

(b) : Point with the best convexity.

Figure 5.11: Current density generating two Pareto-optimal points in figure 5.9.

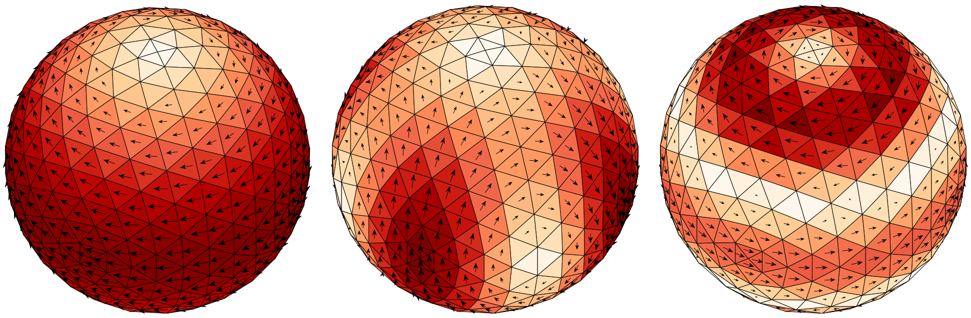

(a) : Current density generating magnetic field along z-axis.

(b) : Current density generating the first derivative along x-axis of the y-component of magnetic field and the first derivative along y-axis of the x-component magnetic field. These components are equal thanks to (3.8).

(c) : Current density generating second derivatives along x, y, z-axes of the z-component of magnetic field, the sum of which is zero thanks to (3.9).

Figure 5.12: Basis current densities composing the optimal current density on a sphere.

The decomposition of the optimal current density into the basis generated by the generalized eigenvalue problem (4.55) can be performed on arbitrarily shaped current supports. Compared to a spherical surface, their linear combination forming an optimal current density (see figure 5.13 for nonspherical examples) is, however, more complicated and the basis currents can not be split into independent subspecies generating the magnetic field, its first or second derivatives.

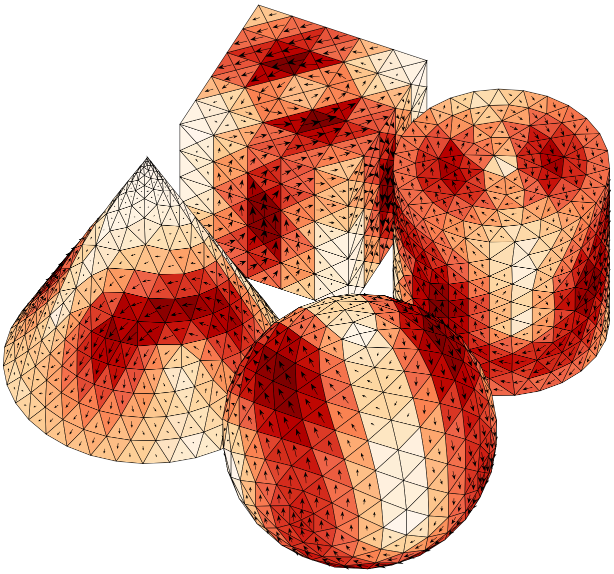

Figure 5.13: Optimal current densities with maximal convexity for different shapes of current supporting region.

5.2.3 Final Comparison

Through all this section, many magnetic traps are mentioned. To compare them, their performance in convexity and potential energy in the trapping center are written in table 5.2, which also contains the values of fundamental bounds for the introduced geometries.

Table 5.2: Performance in convexity and potential energy in the trapping center for all designs of magnetic traps analyzed in this thesis.

Structure	$\frac{a^4 R_s}{\mu_0^2 P_{\text{lost}}} \tilde{\lambda}^{\text{min}}$ (−)	$\frac{\rho^2 R_s}{\mu_0^2 P_{\text{lost}}} B^2$ (−)
Sphere	$1.23 \cdot 10^{-1}$	$1.04 \cdot 10^{-1}$
Cylinder	$7.35 \cdot 10^{-2}$	$9.12 \cdot 10^{-2}$
Cube	$6.04 \cdot 10^{-2}$	$6.65 \cdot 10^{-2}$
Baseball 17°	$4.02 \cdot 10^{-3}$	$6.97 \cdot 10^{-3}$
Baseball 22°	$1.82 \cdot 10^{-2}$	$3.16 \cdot 10^{-3}$
1. Ioffe-Pritchard	$3.88 \cdot 10^{-3}$	$8.91 \cdot 10^{-4}$
2. Ioffe-Pritchard	$5.67 \cdot 10^{-4}$	$1.40 \cdot 10^{-3}$
3. Ioffe-Pritchard	$1.88 \cdot 10^{-3}$	$1.13 \cdot 10^{-3}$
Hexapole	0	0
Quadrupole “Bergeman”	$4.77 \cdot 10^{-3}$	0
Quadrupole “Ríos”	$3.02 \cdot 10^{-3}$	0

As can be seen in the table, realizations performance in given metrics is quite far from their fundamental bounds, which implies the necessity of their optimization and improvement to get closer to these limit values. An important realization is also that quadrupole traps provide comparatively good performance in localization of particles, having higher Hessian matrix eigenvalues than all introduced Ioffe-Pritchard magnetic traps.

Although the baseball traps in figure 5.9 are obviously similar to optimal current densities in figure 5.11, their performance is almost ten times lower than the fundamental bound to magnetic confinement for a sphere. Figure 5.5 with space distribution of confinement potential generated by baseball traps shows that the weakest convexity is along z-axis. This can serve as a guide for further improvement. Performance of Ioffe-Pritchard traps is lower compared to baseball traps. It is probably the simplicity of design which however makes them popular.

Chapter 6

Conclusion

The aim of the thesis was to get acquainted with the principles of magnetic levitation, magnetic confinement, and their classical quasi-static description, propose scalar metrics to judge their performance, describe quasi-static electromagnetic field via electric field integral equation (EFIE) formulated in method of moments (MoM) formalism and use Rao-Wilton-Glisson (RWG) basis functions over a triangular mesh. The last goal was to formulate and evaluate fundamental bounds on the performance of the proposed scalar metrics and compare them with the performance of existing devices. The thesis addressed all these tasks, dividing the work into several individual steps.

Firstly, important assumptions and restrictions, greatly reducing the mathematical complexity but having only insignificant impact on the generality of the description and its applicability, were introduced. The major one was the application of the second-order Taylor polynomial expansion to the potential energy, which later allowed for problem description using quadratic forms.

Secondly, the magnetic levitation and magnetic confinement problems were analysed by the second-order Taylor polynomial expansion of potential energy at the desired point for levitation or confinement. The first three terms of the Taylor polynomial were used to propose a scalar metric to judge the performance of devices for magnetic levitation and magnetic confinement. The optimization problems generating fundamental bounds were established.

Thirdly, the computational tools of mathematical physics such as the formulation of magnetic field and its derivatives through the expansion of the current density into a set of basis functions with the use of MoM, EFIE description of electromagnetic field and QCQP were introduced. Furthermore, apropriate entire-domain basis functions were derived from field integral description of electromagnetic field. This set of the basis functions is suitable for representation of stationary current density on metallic objects excited by sources under quasi-static conditions. The optimization problems to fundamental bounds were rewritten employing the expansion of current density and MoM to a QCQP.

Lastly, the tools were applied to assess the performance of common devices for magnetic levitation and magnetic confinement and to evaluate the fundamental bounds. The outcomes and results were compared and discussed implying interesting questions for further study.

6.1 Further Studies

Since the thesis addressed many attractive questions regarding fundamental bounds on magnetic levitation and magnetic confinement, it also induced several important questions and topics for further research which are briefly commented in this section.

Chapter 5 in tables 5.1, 5.2 showed that the commonly used levitators and magnetic traps perform far from the corresponding fundamental bounds. This observation calls for an improvement of these practical realizations being inspired by the shape of the optimal current density. A future goal is also to employ topology optimization and produce magnetic traps and levitators with significantly higher performance than those known in the literature.

The optimization problem for fundamental bounds on magnetic levitation and magnetic confinement introduced in sections 4.3.1, 4.3.2 uses an assumption of diagonal Hessian matrix and equal diagonal terms which results in isotropic potential wells. An interesting question is what would be the result if the Hessian matrix did not have to satisfy these assumptions and directly the minimal eigenvalue was maximized as described in sections 3.1, 3.2. Would the fundamental bounds generated by this general optimization be significantly higher than those described in the thesis or would they be close to each other? The further goal is to implement such generalized optimization for fundamental bounds and compare its results with those from the thesis.

More generally, what would be the result, if the local criteria for the potential well given by the second-order Taylor polynomial expansion in the center of the potential well were not used and the trap depth was measured by the difference between the minimal potential energy in the trap and its lowest threshold[1] (minimal potential energy on the boundary of the potential well)? Algorithm for searching the global threshold will be rather complex

---

[1] Commonly used measure of trap's depth is temperature of particles which remain confined by the trap, $T = \Phi_\Delta / k_\mathrm{B}$, where Φ_Δ is potential energy difference between the lowest threshold and the trap minimum, k_B is the Boltzmann constant [19].

as it is generally difficult to find the threshold in three dimensions. This metric would however be useful for the global comparison of magnetic traps and devices for levitation with the advantage that it could be applied to all devices[2].

Another interesting question is the difference between the fundamental bounds on magnetic levitation and magnetic confinement for the current supporting region in a form of surface and volume. Can the performance of volumetric supporting regions significantly improve the performance? For example, what is the difference between the fundamental bounds for confinement with surface current distributed on a spherical shell or volumetric current distributed in a spherical layer?

The relation to vector spherical harmonics shown in appendix B also offers an attractive topic and implies some questions, mainly if it is possible to find the fundamental bound on confinement for the sphere analytically? How do the higher-order spherical vector harmonics on a spherical shell influence the potential near the trapping center?

Magnetic traps with multiple trapping centers are in practice used to confine different atomic species [35]. The description given in sections 3.2, 4.3.2 can be easily expanded for multiple trapping centers and similarly can be expanded the current density subspace for their optimization shown in appendix B. The expansion can serve to find fundamental bounds for confining particles in multiple trapping centers, which might be the focus of further studies with practical impact.

---

[2] This approach would allow to compare also hexapole trap with other realizations or with fundamental bounds which was not possible within the approximation via the second-order Taylor polynomial

Appendix A

Evaluation of Magnetic Field Operators

This appendix introduces Rao-Wilton-Glisson (RWG) function defined on a triangular mesh[1], which is used as primary basis for surface current density and magnetic field operators introduced in section 4.1 and for impedance matrix introduced in section 4.2. Within this thesis, RWG functions are used as basis and testing functions in MoM solution to EFIE, see [23, 24], [36, section 8.2] for more details.

A.1 Rao-Wilton-Glisson (RWG) function

RWG function is defined for a triangular mesh as

$$\boldsymbol{\psi}_n(\boldsymbol{r}) = \begin{cases} \dfrac{L_n}{2A_n^+}\boldsymbol{\rho}_n^+(\boldsymbol{r}), & \boldsymbol{r} \in T_n^+ \\[2ex] \dfrac{L_n}{2A_n^-}\boldsymbol{\rho}_n^-(\boldsymbol{r}), & \boldsymbol{r} \in T_n^- \\[2ex] 0, & \text{otherwise,} \end{cases} \tag{A.1}$$

where T_n^+ and T_n^- is a pair of adjacent triangles sharing a common edge e_n with length L_n, see figure A.1. Vector $\boldsymbol{\rho}_n^+(\boldsymbol{r})$ is oriented towards the vertex $\mathbf{V}_n^+$, i.e.,

$$\boldsymbol{\rho}_n^+(\boldsymbol{r}) = \mathbf{V}_n^+ - \boldsymbol{r}, \quad \boldsymbol{r} \in T_n^+, \tag{A.2}$$

while, vector $\boldsymbol{\rho}_n^-(\boldsymbol{r})$ points away from the vertex $\mathbf{V}_n^-$, i.e.,

$$\boldsymbol{\rho}_n^-(\boldsymbol{r}) = \mathbf{V}_n^- - \boldsymbol{r}, \quad \boldsymbol{r} \in T_n^-. \tag{A.3}$$

---

[1] RWG functions are the most commonly used basis functions in MoM solution to surface EFIE since its introduction in 1982 [36, section 8.2].

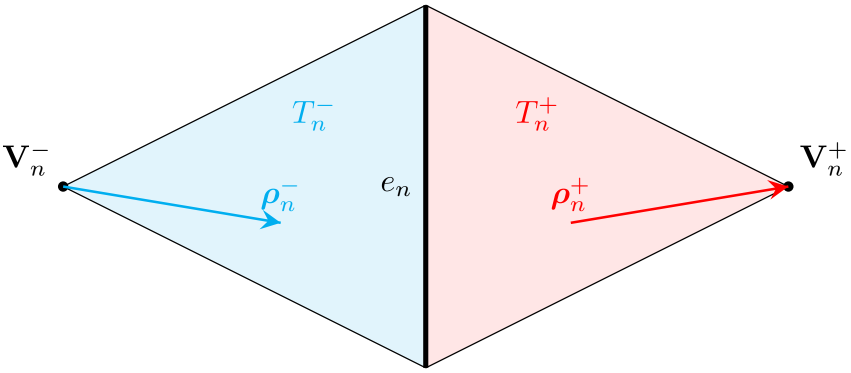

Figure A.1: Illustration of RWG function.

A.2 Magnetic Field Operators in a Set of Basis Functions

This section introduces the numerical implementation of the magnetic field and its first and second spatial derivatives in a set of basis functions $\{\boldsymbol{\psi}_n\}$. The implementation involves a numerical quadrature [37], the prototype of which reads

$$\int\limits_{T_n^+\cup T_n^-} \boldsymbol{\psi}_n(\boldsymbol{r}') \times \frac{\boldsymbol{R}(\boldsymbol{r},\boldsymbol{r}')}{|\boldsymbol{R}(\boldsymbol{r},\boldsymbol{r}')|^3}\,\mathrm{d}S' \approx \sum_m w_m \boldsymbol{\psi}_n(\boldsymbol{r}_m) \times \frac{\boldsymbol{R}_m(\boldsymbol{r})}{|\boldsymbol{R}_m(\boldsymbol{r})|^3} \tag{A.4}$$

where the separation vector

$$\boldsymbol{R}_m(\boldsymbol{r}) = \boldsymbol{r} - \boldsymbol{r}_m, \tag{A.5}$$

is defined and w_m are weights of quadrature points (QPs) $\boldsymbol{r}_m$. For the particular set of QPs and weights for triangular domains see [37].

Suppose substitution

$$\boldsymbol{g}_m(\boldsymbol{r}) = \frac{\boldsymbol{R}_m(\boldsymbol{r})}{|\boldsymbol{R}_m(\boldsymbol{r})|^3} \tag{A.6}$$

per each QP. Then, the Biot-Savart formula (4.1), with current density expanded in a set of basis functions, reads

$$\boldsymbol{B}(\boldsymbol{r}) \approx \frac{\mu_0}{4\pi} \sum_{n=1}^{N} I_n \sum_m w_m \boldsymbol{\psi}_n(\boldsymbol{r}_m) \times \boldsymbol{g}_m(\boldsymbol{r}). \tag{A.7}$$

The same procedure is applied to derivatives (4.8), (4.9), which are then evaluated as

$$\frac{\partial \boldsymbol{B}}{\partial i} = \frac{\mu_0}{4\pi} \sum_{n=1}^{N} I_n \sum_m w_m \boldsymbol{\psi}_n(\boldsymbol{r}_m) \times \frac{\partial \boldsymbol{g}_m(\boldsymbol{r})}{\partial i}, \tag{A.8}$$

$$\frac{\partial^2 \boldsymbol{B}}{\partial j \partial i} = \frac{\mu_0}{4\pi} \sum_{n=1}^{N} I_n \sum_m w_m \boldsymbol{\psi}_n(\boldsymbol{r}_m) \times \frac{\partial^2 \boldsymbol{g}_m(\boldsymbol{r})}{\partial j \partial i}, \tag{A.9}$$

where the first derivative of the substituted function reads component-wise

$$\frac{\partial g_{m,i}(\boldsymbol{r})}{\partial_j} = \begin{cases} \dfrac{1}{|\boldsymbol{R}_m(\boldsymbol{r})|^3} - 3\dfrac{(r_i - r_{m,i})^2}{|\boldsymbol{R}_m(\boldsymbol{r})|^5}, & i = j, \\ -3\dfrac{(r_i - r_{m,i})(r_j - r_{m,j})}{|\boldsymbol{R}_m(\boldsymbol{r})|^5}, & i \neq j, \end{cases} \tag{A.10}$$

and second derivatives with interchangeability of derivatives taken into account read component-wise

$$\frac{\partial^2 g_{m,i}(\boldsymbol{r})}{\partial k \partial j} = \begin{cases} 15\dfrac{(r_i - r_{m,i})^3}{|\boldsymbol{R}_m(\boldsymbol{r})|^7} - 9\dfrac{(r_i - r_{m,i})^3}{|\boldsymbol{R}_m(\boldsymbol{r})|^5}, & i = j = k, \\ 15\dfrac{(r_j - r_{m,j})^2(r_i - r_{m,i})}{|\boldsymbol{R}_m(\boldsymbol{r})|^7} - 3\dfrac{(r_i - r_{m,i})^3}{|\boldsymbol{R}_m(\boldsymbol{r})|^5}, & i \neq j = k, \\ 15\dfrac{(r_i - r_{m,i})^2(r_k - r_{m,k})}{|\boldsymbol{R}_m(\boldsymbol{r})|^7} - 3\dfrac{(r_k - r_{m,k})^3}{|\boldsymbol{R}_m(\boldsymbol{r})|^5}, & i = j \neq k, \\ 15\dfrac{(r_i - r_{m,i})(r_j - r_{m,j})(r_k - r_{m,k})}{|\boldsymbol{R}_m(\boldsymbol{r})|^7}, & i \neq j \neq k. \end{cases} \tag{A.11}$$

Finally, matrices for the magnetic field and its first, second spatial derivatives (4.4) – (4.9) can be evaluated element-wise as

$$\mathbf{B}_n = \frac{\mu_0}{4\pi} \sum_m w_m \boldsymbol{\psi}_n(\boldsymbol{r}_m) \times \boldsymbol{g}_m(\boldsymbol{r}), \tag{A.12}$$

$$\mathbf{B}_{n,i} = \frac{\mu_0}{4\pi} \sum_m w_m \boldsymbol{\psi}_n(\boldsymbol{r}_m) \times \frac{\partial \boldsymbol{g}_m(\boldsymbol{r})}{\partial i}, \tag{A.13}$$

$$\mathbf{B}_{n,ij} = \frac{\mu_0}{4\pi} \sum_m w_m \boldsymbol{\psi}_n(\boldsymbol{r}_m) \times \frac{\partial^2 \boldsymbol{g}_m(\boldsymbol{r})}{\partial j \partial i}. \tag{A.14}$$

Appendix B

Minimal Subset of Currents on a Spherical Shell

In this appendix, the entire domain basis functions significant to magnetic potential energy operators in the centre of a sphere, eigenvectors corresponding to non-zero eigenvalues in (4.55), are shown and analyzed. The geometry of a sphere and the investigated point in its centre simplifies the presentation and offers mutually orthogonal subspaces to the magnetic field and its derivatives. The decomposition can nevertheless be done for any shape of current support and any point in space. In a general scenario, the aforementioned orthogonality is however lost.

If eigenvalue problem (4.55) is applied directly on operators projected to RWG basis, the dimension of resulting sub-basis is 23, thanks to constraints (3.7)–(3.9). If the eigenvalue problem (4.55) is applied after conducting "Loop-Star" decomposition introduced in section 4.2.1 and all considered matrices are mapped onto the basis given by solenoidal current densities in (4.31), the resulting sub-basis dimension is only 15. This later linearly independent set is the topic of this chapter.

For a sphere and investigated point in its centre, the sub-basis of 15 vectors closely reassemble vector spherical harmonics [38, appendix C.4], which are defined as

$$\boldsymbol{A}_{1\sigma ml}(\boldsymbol{r}_0) = \frac{1}{\sqrt{l(l+1)}} \nabla \times [\boldsymbol{r} Y_{\sigma ml}(\boldsymbol{r}_0)] = \frac{1}{\sqrt{l(l+1)}} \nabla Y_{\sigma ml}(\boldsymbol{r}_0) \times \boldsymbol{r}, \tag{B.1}$$

$$\boldsymbol{A}_{2\sigma ml}(\boldsymbol{r}_0) = \frac{1}{\sqrt{l(l+1)}} r \nabla Y_{\sigma ml}(\boldsymbol{r}_0), \tag{B.2}$$

$$\boldsymbol{A}_{3\sigma ml}(\boldsymbol{r}_0) = \boldsymbol{r}_0 Y_{\sigma ml}(\boldsymbol{r}_0), \tag{B.3}$$

where $\boldsymbol{r}$ is radial vector, $\boldsymbol{r}_0$ is unit vector along $\boldsymbol{r}$ and bottom index $\sigma \in \{\mathrm{e}, \mathrm{o}\}$ determines the spherical harmonic $Y_{\sigma ml}$ to be even[1] ($\sigma = \mathrm{e}$) or odd ($\sigma =$

---

[1] If order $m = 0$, then spherical harmonic is always even.

o). The indices $m \in \{0, 1, \dots, l\}$ and $l \in \{0, 1, \dots\}$ denote the degree and order of spherical harmonics, respectively. The vector spherical harmonics $\boldsymbol{A}_{1\sigma ml}$, $\boldsymbol{A}_{2\sigma ml}$ are perpendicular to radial vector, while the vector spherical harmonic $\boldsymbol{A}_{3\sigma ml}$ is parallel to radial vector. Since the current density flows on the surface of a sphere and since only currents with stored magnetic energy dominating over stored electric energy are used, vector spherical harmonics $\boldsymbol{A}_{1\sigma ml}$ (TE waves) will solely be needed.

The sub-basis can be divided into three main groups:

- Current densities generating only magnetic field in the centre of the sphere, but exhibiting vanishing first and second spatial derivatives. Since the magnetic field operator (4.4) has three linearly independent rows, these current densities are also three. These current densities are shown in figure B.1.Via this set, an arbitrary magnetic field in the centre of the sphere can be generated. The three depicted current densities reassemble vector spherical harmonics $\boldsymbol{A}_{1\sigma m1}$, $m \in \{0, 1\}$.

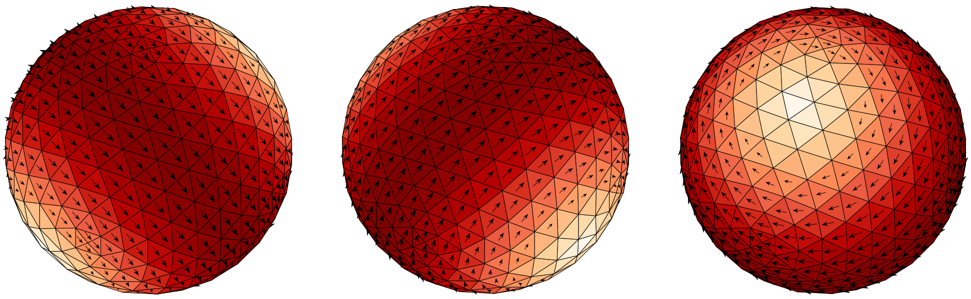

Figure B.1: Current densities generating magnetic field in the center of the sphere. The only differenc between the plotted currentsities, vector spherical harmonic is their orientation in space, they are arbitrarily rotated in space.

- Current densities forming the first spatial derivative of the magnetic field in the centre of the sphere. The operators describing the first derivatives of magnetic field (4.8) are composed of nine different rows, however, they are linearly dependent and the first derivatives of the magnetic field in the centre of the sphere can fully be controlled by only five current densities, which corresponds to certain combinations of vector spherical harmonics $\boldsymbol{A}_{1\sigma m2}$, $m \in \{0, 1, 2\}$. The current densities can be found in figure B.2.
- Current densities forming second spatial derivatives of the magnetic field in the centre of the sphere. There are 18 rows forming the magnetic field second derivative operator (4.9) from which only seven are independent. These resemble vector spherical harmonics $\boldsymbol{A}_{1\sigma m3}$, $m \in \{0, 1, 2, 3\}$ and are depicted in figure B.3.

In the case of a sphere and inspected point in its centre the combination

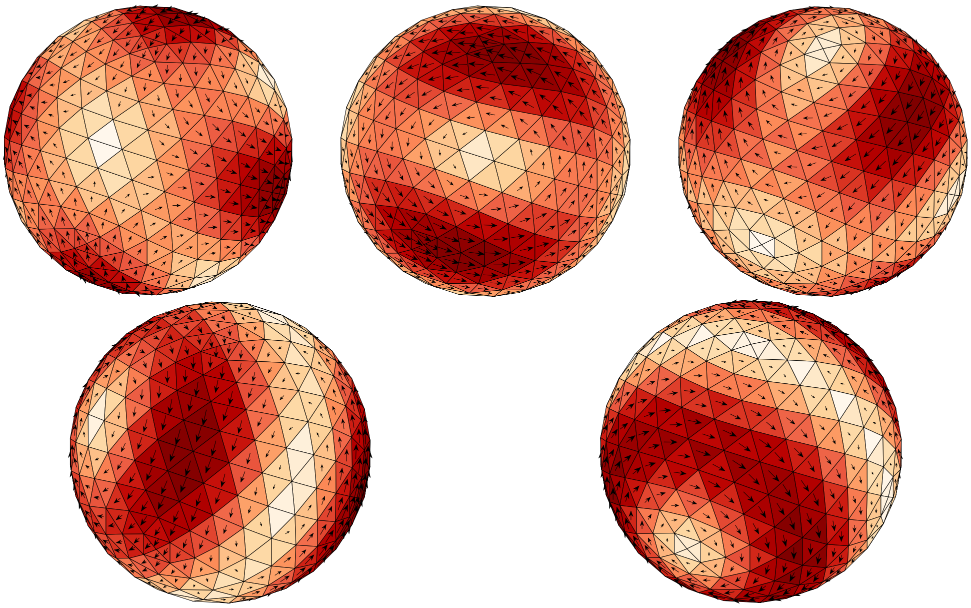

Figure B.2: Current densities generating first spatial derivatives of magnetic field in the center of the sphere. Each row of the figure contains similar vector spherical harmonics differently rotated in space.

of vector spherical harmonics from figures B.1–B.3 produces currents with optimal performance. This property results from the spherical symmetry of the configuration. For different geometries of the current density support or position of the inspected point, higher-order vector spherical harmonics have to be used to obtain optimal performance. The significance of higher-order waves nevertheless decreases fast with increasing degree l.

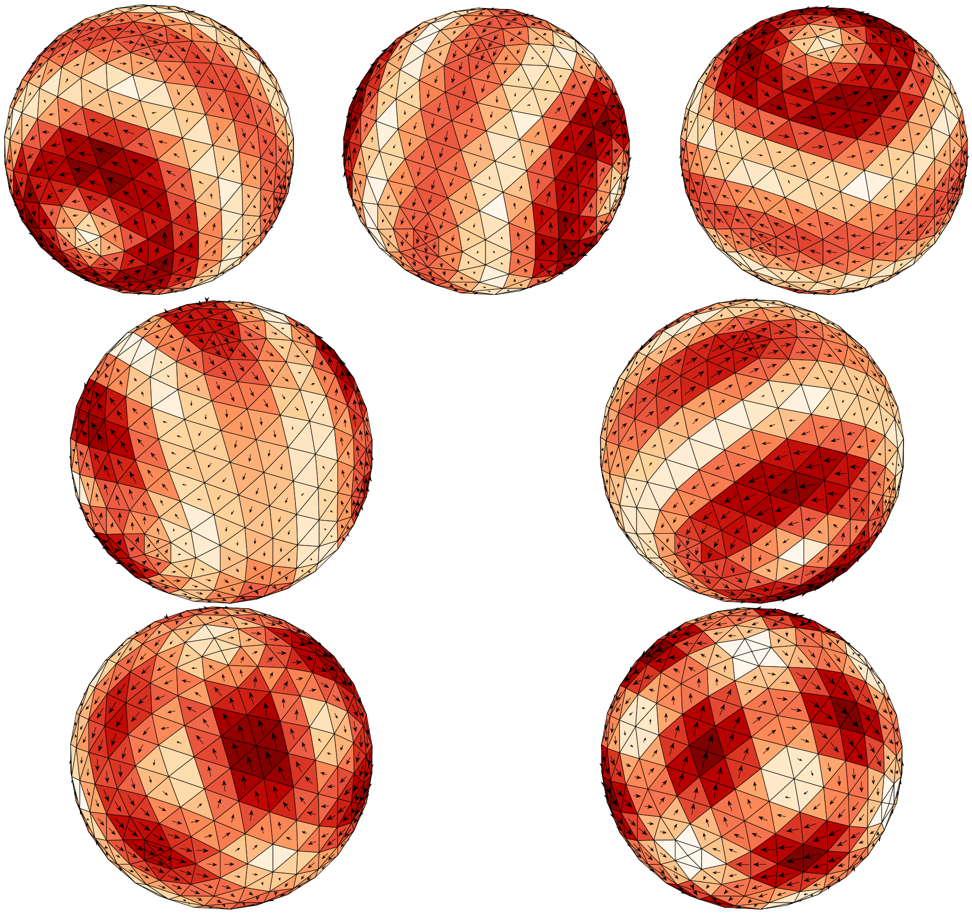

Figure B.3: Current densities generating second spatial derivatives of magnetic field in the center of the sphere. Each row of the figure contains similar vector spherical harmonics differently rotated in space.

Appendix C

Bibliography

[1] F. C. Moon, *Superconducting levitation : applications to bearings and magnetic transportation.* New York: Wiley, 1994.

[2] V. S. Nikolayev, D. Chatain, D. Beysens, and G. Pichavant, “Magnetic gravity compensation,” *Microgravity Science and Technology*, vol. 23, pp. 113–122, jul 2010.

[3] E. H. BRANDT, “Levitation in physics,” *Science*, vol. 243, pp. 349–355, jan 1989.

[4] H.-W. Lee, K.-C. Kim, and J. Lee, “Review of maglev train technologies,” *IEEE Transactions on Magnetics*, vol. 42, pp. 1917–1925, jul 2006.

[5] P. C. Nordine and R. M. Atkins, “Aerodynamic levitation of laser-heated solids in gas jets,” *Review of Scientific Instruments*, vol. 53, pp. 1456–1464, sep 1982.

[6] M. Palmer, “Affordable air - vertical wind tunnel for indoor skydiving,” in *38th Aerospace Sciences Meeting and Exhibit*, American Institute of Aeronautics and Astronautics, jan 2000.

[7] J. K. R. Weber, C. A. Rey, J. Neuefeind, and C. J. Benmore, “Acoustic levitator for structure measurements on low temperature liquid droplets,” *Review of Scientific Instruments*, vol. 80, p. 083904, aug 2009.

[8] A. Ashkin and J. M. Dziedzic, “Observation of light scattering from nonspherical particles using optical levitation,” *Applied Optics*, vol. 19, p. 660, mar 1980.

[9] J. Pérez-Ríos and A. S. Sanz, “How does a magnetic trap work?,” *American Journal of Physics*, vol. 81, pp. 836–843, nov 2013.

[10] M. D. Simon and A. K. Geim, “Diamagnetic levitation: Flying frogs and floating magnets (invited),” *Journal of Applied Physics*, vol. 87, pp. 6200–6204, may 2000.

[11] W. D. Phillips, “Nobel lecture: Laser cooling and trapping of neutral atoms,” *Reviews of Modern Physics*, vol. 70, pp. 721–741, jul 1998.

[12] A. Zangwill, *Modern electrodynamics.* Cambridge University Press, 2013.

[13] A. Geim, “Everyone's magnetism,” *Physics Today*, vol. 51, pp. 36–39, sep 1998.

[14] M. V. Berry and A. K. Geim, “Of flying frogs and levitrons,” *European Journal of Physics*, vol. 18, pp. 307–313, jul 1997.

[15] A. E. Leanhardt, “Cooling bose-einstein condensates below 500 picokelvin,” *Science*, vol. 301, pp. 1513–1515, sep 2003.

[16] P. Lax, *Multivariable calculus with applications.* Cham: Springer, 2017.

[17] J. Stewart, *Multivariable calculus : concepts and contexts.* Belmont, CA: Thomson Brooks/Cole, 2005.

[18] S. Gov, S. Shtrikman, and H. Thomas, “Magnetic trapping of neutral particles: Classical and quantum-mechanical study of a ioffe–pritchard type trap,” *Journal of Applied Physics*, vol. 87, pp. 3989–3998, apr 2000.

[19] T. Bergeman, G. Erez, and H. J. Metcalf, “Magnetostatic trapping fields for neutral atoms,” *Physical Review A*, vol. 35, pp. 1535–1546, feb 1987.

[20] V. I. Arnol’d, *Mathematical methods of classical mechanics.* New York, NY: Springer, 1989.

[21] D. Lay, *Linear algebra and its applications.* Boston: Pearson, 2016.

[22] J. David Jackson, *Classical Electrodynamics, 3rd Edition.* Wiley-IEEE Press, 07 1998.

[23] S. M. Rao, D. R. Wilton, and A. W. Glisson, “Electromagnetic scattering by surfaces of arbitrary shape,” *Antennas and Propagation, IEEE Transactions on*, vol. 30, pp. 409 – 418, 06 1982.

[24] R. F. Harrington, *Field Computation By Moment Method.* Wiley-IEEE Press, 01 1993.

[25] MATLAB, “version 9.9.0.1592791 (R2020b) Update 5.” online, Sept. 2020.

[26] R. Harrington, “Antenna excitation for maximum gain,” *IEEE Transactions on Antennas and Propagation*, vol. 13, pp. 896–903, nov 1965.

[27] G. Vecchi, “Loop-star decomposition of basis functions in the discretization of the EFIE,” *IEEE Transactions on Antennas and Propagation*, vol. 47, no. 2, pp. 339–346, 1999.

[28] J. Nocedal and S. J. Wright, *Numerical Optimization.* Springer, 01 2006.

[29] S. Boyd, *Convex optimization.* Cambridge University Press, 2004.

[30] P. Ngatchou, A. Zarei, and A. El-Sharkawi, "Pareto multi objective optimization," in *Proceedings of the 13th International Conference on, Intelligent Systems Application to Power Systems*, IEEE, 2005.

[31] H. Chetouani, B. Delinchant, and G. Reyne, "Efficient modeling approach for optimization of a system based on passive diamagnetic levitation as a platform for bio-medical applications"," *COMPEL: The International Journal for Computation and Mathematics in Electrical and Electronic Engineering*, vol. 26, no. 2, pp. 345 – 355, 2007.

[32] W. Petrich, M. H. Anderson, J. R. Ensher, and E. A. Cornell, "Stable, tightly confining magnetic trap for evaporative cooling of neutral atoms," *Physical Review Letters*, vol. 74, pp. 3352–3355, apr 1995.

[33] C. V. Sukumar and D. M. Brink, "Spin-flip transitions in a magnetic trap," *Physical Review A*, vol. 56, pp. 2451–2454, sep 1997.

[34] F. J. López-López, "Question ♯48. is there a physical property that determines the curve which defines the seam of a baseball?," *American Journal of Physics*, vol. 64, pp. 1097–1097, sep 1996.

[35] J. Hu and J. Yin, "Controllable double-well magnetic traps for neutral atoms," *Journal of the Optical Society of America B*, vol. 19, p. 2844, dec 2002.

[36] W. C. Gibson, *The Method of Moments in Electromagnetics*, vol. 1. CRC Press/Taylor & Francis, second ed., 2015.

[37] J. A. Reeger, B. Fornberg, and M. L. Watts, "Numerical quadrature over smooth, closed surfaces," *Proceedings of the Royal Society A: Mathematical, Physical and Engineering Sciences*, vol. 472, p. 20160401, oct 2016.

[38] G. Kristensson, *Scattering of Electromagnetic Waves by Obstacles.* Stevenage: The Institution of Engineering and Technology, 2016.

MASTER‘S THESIS ASSIGNMENT

I. Personal and study details

Student's name: **Liška Jakub** Personal ID number: **466385**

Faculty / Institute: **Faculty of Electrical Engineering**

Department / Institute: **Department of Radioelectronics**

Study program: **Open Electronic Systems**

Branch of study: **RF and DSP Engineering**

II. Master’s thesis details

Master’s thesis title in English:

Fundamental Bounds on Magnetic Levitation and Magnetic Confinement

Master’s thesis title in Czech:

Principiální omezení magnetické levitace a magnetického zadržování

Guidelines:

Get acquainted with principles of magnetic levitation and magnetic confinement and their classical quasi-static description. Propose scalar metrics that can be used to judge the performance of magnetic traps and magnetic levitation devices. Describe quasi-static electromagnetic field in these processes via electric field integral equation formulated in method-of-moments formalism. Use surface impedance model and Rao-Wilton-Glisson basis functions over triangular mesh. In the second stage, formulate and evaluate fundamental bounds on performance of magnetic levitation and magnetic confinement. Compare performance of existing devices with the corresponding bounds.

Bibliography / sources:

[1] S. Gov and S. Shtrikman, “Magnetic trapping of neutral particles: Classical and quantum-mechanical study of a Ioffe–Pritchard type trap”, Journal of Applied Physics Vol. 87, p. 3989, 2000.
[2] J. Perez-Riosa, “How does a magnetic trap work?”, American Journal of Physics, Vol. 81, p. 836, 2013.
[3] R. F. Harrington, Field Computation by Moment Methods, Wiley–IEEE Press, 1993.
[4] S. M. Rao, D. R. Wilton, and A. W. Glisson, “Electromagnetic scattering by surfaces of arbitrary shape,” IEEE Transaction on Antennas and Propagation, Vol. 30, pp. 409 – 418, 1982.
[5] J. Nocedal and S. Wright, Numerical Optimization, New York, Springer, 2006.

Name and workplace of master’s thesis supervisor:

doc. Ing. Lukáš Jelínek, Ph.D., Department of Electromagnetic Field, FEE

Name and workplace of second master’s thesis supervisor or consultant:

Date of master’s thesis assignment: **21.01.2021** Deadline for master's thesis submission: ___________

Assignment valid until: **30.09.2022**

doc. Ing. Lukáš Jelínek, Ph.D. Supervisor’s signature	doc. Ing. Josef Dobeš, CSc. Head of department’s signature	prof. Mgr. Petr Páta, Ph.D. Dean’s signature

III. Assignment receipt

The student acknowledges that the master’s thesis is an individual work. The student must produce his thesis without the assistance of others, with the exception of provided consultations. Within the master’s thesis, the author must state the names of consultants and include a list of references.

Date of assignment receipt	Student’s signature